



Dynamics of upwelling in the Alaskan Beaufort Sea and associated shelf–basin fluxes



Robert S. Pickart^{a,*}, Michael A. Spall^a, Jeremy T. Mathis^b

^a Woods Hole Oceanographic Institution, Woods Hole, MA 02540, USA

^b NOAA Pacific Marine Environmental Laboratory, Seattle, WA 98115, USA

ARTICLE INFO

Article history:

Received 25 May 2012

Received in revised form

3 January 2013

Accepted 23 January 2013

Available online 8 February 2013

Keywords:

Upwelling

Boundary currents

Shelf–basin interaction

Pack-ice

ABSTRACT

Data from a high-resolution mooring array deployed across the Alaskan Beaufort shelfbreak and slope, together with an idealized numerical model, are used to investigate the dynamics of wind-driven upwelling and the magnitude of the resulting shelf–basin exchange. The analysis focuses on a single storm event in November 2002 when the sea-ice concentration was 50–70%. The normally eastward-flowing shelfbreak jet was reversed to the west, and the secondary circulation near the shelfbreak was characterized by offshore flow in the upper layer and a nearly equal amount of onshore flow at depth. Ekman theory accurately predicts the strength of the secondary circulation when one takes into account the ice–ocean stress. The depth-integrated alongstream momentum balance reveals that, near the shelf edge, the reversed jet is driven by a combination of the surface stress and divergence of cross-stream momentum flux. The reversed jet is primarily spun-down – before the winds subside – by the alongstream pressure gradient that likely results from the variation in sea surface height. The shelf–basin fluxes of heat, freshwater, and nitrate resulting from the storm are substantial. Much of the yearly supply of heat to the Beaufort shelf from the inflowing Pacific water through Bering Strait was fluxed offshore, and the amount of freshwater transported into the basin represents a substantial fraction of the year-to-year variation in the freshwater inventory of the Beaufort Gyre. The on-shelf flux of nitrate from 4 to 5 such storms could account for most of the net annual primary production that occurs on the Beaufort shelf.

© 2013 Elsevier Ltd. All rights reserved.

1. Introduction

Two types of storms are known to influence the Alaskan Beaufort Sea: Arctic-born storms and Pacific-born storms. The former enter the region from the north and result in westerly winds along the Beaufort shelf and slope. The ensuing ocean currents and energetic waves can lead to significant coastal erosion along the North Slope of Alaska (e.g. Lynch et al., 2004). The latter type of storm develops well to the south in the Pacific Ocean. These low pressure systems tend to intensify in the region of the Aleutian Island chain, and are commonly referred to as “Aleutian Lows” (e.g. Wilson and Overland, 1986; Pickart et al., 2009a). Due in part to their broad extent, Aleutian lows can also influence the Beaufort shelf and slope, but the winds in this case are out of the east. The Arctic-born storms are thus downwelling favorable, while the Pacific-born storms are upwelling favorable. Although either type of storm can occur during any month of the year, the Arctic storms are most common in late-summer and

early-fall, and the Aleutian Lows are most frequent in late-fall and winter. It should be noted that these storm events are distinct from the general easterly atmospheric flow in the southern Canada Basin associated with the Beaufort High. Not surprisingly, in the mean the winds in the Alaskan Beaufort Sea are from the east (Furey, 1996).

The prevailing ocean circulation on the Alaskan Beaufort outer shelf and slope is to the east, i.e. in opposition to the mean winds (e.g. Aagaard, 1984; Pickart, 2004; Nikolopoulos et al., 2009). The reason for this is that a portion of the Pacific water that enters the Arctic through the Bering Strait (driven by the Pacific/Atlantic sea-level gradient) eventually rounds Pt. Barrow and heads towards the Canadian Beaufort (Fig. 1). The majority of this flow is contained within a narrow jet at the edge of the shelf, known as the Beaufort shelfbreak jet or western Arctic boundary current (Pickart, 2004; Nikolopoulos et al., 2009). This jet resides shoreward of and shallower than the eastward-flowing Atlantic Water that is part of the Arctic-wide cyclonic boundary current system (e.g. Rudels et al., 1994; Woodgate et al., 2001; Karcher et al., 2007; Aksenov et al., 2011). The Beaufort shelfbreak jet has distinct seasonal configurations. In spring and early-summer it transports dense Pacific winter water as a bottom-intensified flow (Spall et al., 2008); in late-summer and

* Corresponding author. Tel.: +1 508 289 2858.

E-mail address: rpickart@whoi.edu (R.S. Pickart).

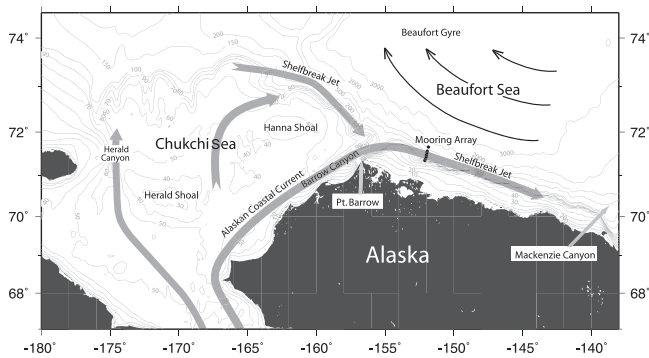


Fig. 1. Schematic circulation of the Chukchi and Beaufort Seas (after Schulze and Pickart, 2012). The locations of the moorings used in the study are indicated by the closed circles. The weather station is located near Pt. Barrow. The bathymetry is the ETOPO-2 product.

early-fall it carries warm Pacific waters and can either be surface-intensified or bottom-intensified (von Appen and Pickart, 2012); and during late-fall and winter the current is again strongest near the bottom and advects cold water (though not as cold as in the spring, Nikolopoulos et al., 2009).

On shorter timescales the Beaufort shelfbreak jet is highly variable. In the absence of wind the current is hydrodynamically unstable. Depending on the time of year, it is either baroclinically unstable or subject to a mixed barotropic/baroclinic instability (Hunkins, 1974; Spall et al., 2008; von Appen and Pickart, 2012). Consequently, the current forms cold-core and warm-core anticyclonic eddies, which populate the interior southern Canada Basin (Plueddemann et al., 1999; Pickart et al., 2005).¹ However, the above-mentioned storms have a strong impact on the shelfbreak jet. The Arctic-born storms accelerate the current to the east and cause downwelling of relatively fresh water (R. Pickart, unpublished data). By contrast, the Pacific-born storms readily reverse the shelfbreak jet to the west (as strong as 1 m s^{-1}) and drive upwelling of subsurface salty water onto the shelf (Pickart et al., 2009b, 2011; Schulze and Pickart, 2012). Over the course of a single year (summer 2002 to summer 2003) the Beaufort shelfbreak jet was impacted by high winds roughly 50% of the time, including 28 upwelling storms and seven downwelling storms (Pickart et al., 2010). Clearly, this part of the western Arctic Ocean is strongly wind-forced.

Due to the unstable nature of the Beaufort shelfbreak jet which results in eddy formation, as well as the secondary (i.e. cross-stream) circulation associated with the storms, the current represents a permeable boundary allowing properties to be exchanged between the shelf and the basin. This has huge ramifications. For example, freshwater from rivers and the Pacific inflow is transferred into the Beaufort Gyre (Proshutinsky, 2009), warm Pacific water spreads offshore which can influence the melting of pack-ice (Steele et al., 2010), and nutrients, carbon, and zooplankton can be exchanged between the shelf and interior which impact the ecosystem (e.g. Mathis et al., 2012; Suydam, 2009; Pickart et al., 2010). It is thus of high importance to understand the mechanisms and dynamics of shelf–basin exchange in the western Arctic, and ultimately quantify the amount of material fluxed across the shelfbreak. This is particularly true as the atmospheric forcing and lateral inputs begin to change in a warming climate. For example, the number of summer Arctic-born storms has increased ten-fold over the last 50 years (J. Walsh, pers. comm., 2006), while the influx of heat and

freshwater through Bering Strait has increased during the past decade (Woodgate et al., 2006). The need to enhance our knowledge of wind-forced shelf–basin exchange in the western Arctic – and of upwelling in particular – forms the motivation for the present study.

This paper investigates the character and dynamics of upwelling in the Alaskan Beaufort Sea using moored and shipboard data and a numerical model. Future studies will address the nature of downwelling events in the shelfbreak jet. The approach is to focus on a single upwelling storm in November 2002, the one previously discussed by Pickart et al. (2011) who considered the local and remote oceanic response to the atmospheric forcing. To provide context for the present analysis, we begin with a brief review of some of the results of Pickart et al. (2011). Next we consider the secondary circulation that results from the storm, including the role of the pack-ice. This is followed by an examination of the vertically-averaged alongstream momentum balance in the shelfbreak jet over the course of the storm, using both the data and model output. Finally, using the data we estimate the wind-driven cross-stream fluxes due to the event, and then investigate parcel trajectories using the model to elucidate the regional-scale impact of such upwelling storms.

2. Data and methods

2.1. Mooring data

The timeseries data used in this study come from a mooring array that was maintained across the Beaufort shelfbreak jet as part of the Western Arctic Shelf–Basin Interactions (SBI) program (Fig. 1). The array was in the water from summer 2002 to summer 2004, and consisted of eight moorings closely spaced across the shelfbreak near 152°W , roughly 150 km to the east of Barrow Canyon (Fig. 2).² Details of the array, data processing, and accuracy of the measurements are found in Spall et al. (2008) and Nikolopoulos et al. (2009). Briefly, the profiling conductivity–temperature–depth (CTD) sensors and combination of acoustic Doppler current profilers (ADCPs) and profiling acoustic travel-time current meters (ACMs) allowed construction of vertical sections of hydrographic variables and alongstream and cross-stream velocity. The primary focus of this study is the vicinity of the shelfbreak and upper continental slope (moorings BS2–BS6 in Fig. 2), for which there were four vertical sections per day of potential temperature, salinity, and potential density, and hourly sections of ADCP velocity. The velocity data were de-tided, and, as discussed in Pickart et al. (2011), the inertial signal due to the storms was significantly smaller than the mesoscale response.

For the storm in question the alongstream direction was chosen objectively, but allowed to vary over the course of the storm. In particular, three different directions were employed: one for the time period immediately before the storm, a second for the period of high winds, and a third for the period immediately after the storm. In each case the alongstream angle was determined by first computing the vertically averaged flow at each of the mooring sites (BS2–BS6, top 250 m of the water column) for the given time period. These vectors were then averaged laterally to obtain a single flow vector whose direction was taken as the alongstream axis. It should be noted this procedure tends to minimize the overall cross-stream transport. The vertical sections of the hydrographic variables and along-stream and cross-stream velocities were constructed on a regular grid using Laplacian-Spline interpolation (see Spall et al., 2008 for

¹ In the northern Canada Basin another class of cold-core eddies is found, thought to emanate from a mid-ocean front (Timmermans et al., 2008).

² The shoreward-most mooring failed in year-one and is not pictured in Fig. 2.

details). The grid spacing was 2 km in the cross-stream direction and 5 m in the vertical for the hydrographic fields and 10 m for the velocity. The ADCPs had a near-surface blanking region ranging from 8 m at mooring BS2 to 45 m at mooring BS6. The hydrographic sampling was limited to the part of the water column deeper than 45 m due to the danger of ice keels damaging the moorings. Much of the analysis presented in the paper uses these gridded data.

The ice concentration timeseries used in the study is the one constructed by Pickart et al. (2009b), i.e. the average concentration in a 35 km (zonal) by 55 km (meridional) box surrounding the array using the AMSR-E data. The ice velocity timeseries at the edge of the shelf (at mooring BS2) is also that computed by Pickart et al. (2009b) using the upward-facing ADCP data at that site. The reader is referred to the detailed discussion in Pickart et al. (2009b) regarding the ice products.

2.2. Shipboard hydrographic and chemical data

During the field phase of SBI, shipboard CTD and water sample data were collected in the vicinity of the 152°W mooring array. In the final part of our study we use data from the hydrographic section that was occupied during the mooring recovery cruise in September 2004. Although this was not coincident with the November 2002 storm (no ships were out that late in the season during SBI), the hydrographic conditions on the shelf and slope were similar during the two time periods. During the cruise a

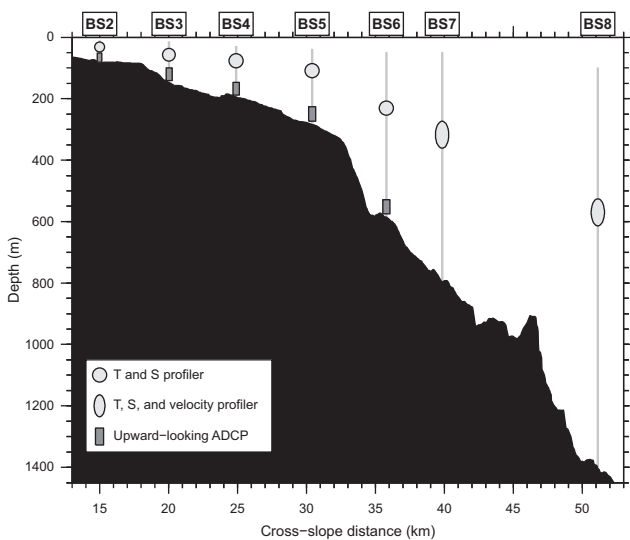


Fig. 2. The SBI Beaufort slope mooring array (from Spall et al., 2008). Mooring names are indicated along the top, and the instrumentation used is listed in the key. The bathymetry is from the shipboard echosounder.

Seabird 911+ CTD was used, which was calibrated using (deep) water sample salinity data following the protocol of the World Ocean Circulation Experiment (WOCE). Resulting accuracies were 0.001 °C for temperature and 0.002 for salinity. In addition to the CTD variables, nutrients were measured from the water samples, as were other chemical properties. Here we use nitrate and dissolved organic carbon (DOC) data to estimate the cross-stream fluxes of these properties. Nutrient samples (nitrate, nitrite, phosphate and silicate) were collected on all CTD casts and analyzed using standardized methods (e.g. Codispoti et al., 2005). Samples for DOC analyses (Mathis et al., 2005) were filtered through in-line precombusted GF/F filters held in acid washed polycarbonate filter holders. Samples were collected into preconditioned and DOC-free, 60 mL HDPE bottles and frozen in organic solvent-free freezers, then shipped to the shore-based laboratories. All DOC samples were analyzed using the Shimadzu TOC-V/TN system. The between-day precision in the DOC measurement was 1 mM, or a CV of 23%.

2.3. Numerical model

The numerical model used in the study is the MIT general circulation model (Marshall et al., 1997). This solves the hydrostatic, primitive equations on a uniform Cartesian, staggered C-grid with level vertical coordinates. A partial cell treatment of the bottom topography is accurate for steep topography in the presence of stratification, expected to be important for the wind-driven upwelling problem (Adcroft et al., 1997).

The model domain is rectangular, extending 2000 km in the zonal direction and 1140 km in the meridional direction, and has closed boundaries on all sides. There is a shelf approximately 35 km wide along the southern boundary that slopes linearly from 40 m at the southern boundary to 100 m at the shelfbreak. The shelf transitions to the open ocean depth of 600 m with a hyperbolic tangent function over a lateral scale of 12 km (Fig. 3a). The horizontal resolution in the region of wind forcing is 4 km in the zonal direction and varies in the meridional direction from 1 km (within 100 km of the southern boundary) to 10 km in the northernmost 800 km of the domain. We have chosen to extend the domain far offshore from the near boundary processes of interest so that the wind-driven response along the northern boundary of the domain and the large-scale geostrophic response to the wind stress do not influence the behavior near the southern boundary. There are 30 levels in the vertical with spacing 5 m between 0 and 100 m, gradually increasing to 150 m spacing between 450 and 600 m depth. Since we are interested in the wind-driven upwelling at depths near the shelfbreak, the model domain is limited to the upper ocean. Density is determined by salinity only and the initial stratification is piecewise uniform in the vertical, $N^2 = 2 \times 10^{-4} \text{ s}^{-2}$ in the upper 175 m and $N^2 = 0.5 \times 10^{-4} \text{ s}^{-2}$ below that (motivated by the observations, see Spall

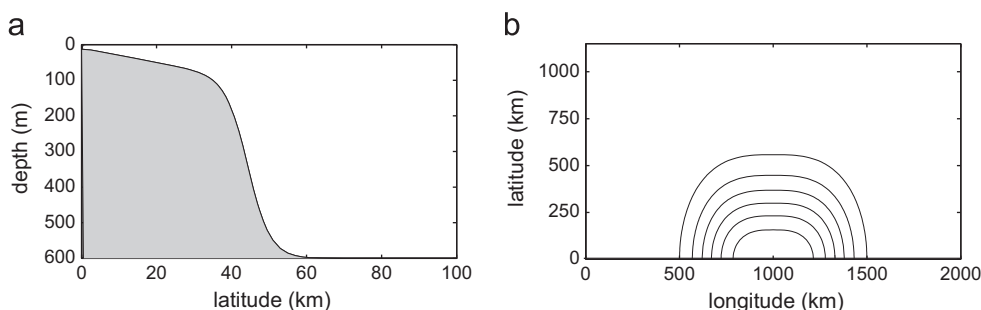


Fig. 3. Model set up. (a) Cross-section of shelf and slope bottom topography near the southern boundary. (b) Zonal wind stress pattern (contour interval of 0.1 N/m²).

et al., 2008). The initial salinity profile (upper 250 m only) is shown in Fig. 12a.

Vertical diffusion of salinity is calculated using the KPP of Large et al. (1994). Horizontal mixing of tracers is parameterized using Laplacian mixing with a coefficient of $10 \text{ m}^2 \text{ s}^{-1}$. The model incorporates second-order vertical viscosity with a coefficient of $10^{-4} \text{ m}^2 \text{ s}^{-1}$. Horizontal viscosity is parameterized with a second order operator with the coefficient A_h determined by a Smagorinsky closure as $A_h = (v_s/\pi)^2 L^2 D$, where v_s is a non-dimensional coefficient taken to be 2 here, L is the grid spacing, and D is the deformation rate, defined as $D = [(u_x - v_y)^2 + (u_y + v_x)^2]^{1/2}$, where u and v are the horizontal velocities and subscripts indicate partial differentiation. A quadratic bottom drag is included with a coefficient of 1.5×10^{-3} . The lateral boundary conditions are no-slip for velocity and no flux for salinity. The qualitative behavior of the model is not overly sensitive to the specific choice of subgridscale mixing.

The model is forced with a zonal wind stress defined as

$$\tau = \tau_0 e^{-(t-t_0)/L_t} e^{-|(x-x_0)/L_x|^3} e^{-|y-y_0|^2/L_y}, \quad (1)$$

where $x_0 = 1000 \text{ km}$ and $y_0 = 0$, $L_x = 400 \text{ km}$ and $L_y = 400 \text{ km}$. The maximum strength $\tau_0 = -0.7 \text{ N/m}^2$ was chosen to impart a comparable surface stress on the ocean as diagnosed at the mooring array. The horizontal pattern of the wind stress is shown in Fig. 3b. The wind spins up over time scale $L_t = 1.5$ days and is a maximum on $t_0 = 2$ days. The model is run for 6 days, and the fields are saved every 0.2 days for the analysis.

3. Wind-driven response of the shelfbreak jet

3.1. Alongstream circulation

In the mean, the Beaufort shelfbreak jet is a narrow (10–15 km width), bottom-intensified current flowing to the east at roughly 15 cm s^{-1} (Fig. 4). It transports both warm and cold Pacific waters towards the Canadian Arctic Archipelago. Synoptically, however, the current and water mass structure can be quite variable and complex, as discussed above. During an upwelling event (easterly winds), the current typically reverses to the west, followed by transport of halocline waters up the continental slope to shallower depths. Typically, Pacific Winter Water from the upper-halocline is advected onto the shelf (Schulze and Pickart, 2012), but, during large events, Atlantic water from the lower halocline can be brought this far onshore. The storm in question occurred in

early November 2002. It was a strong Aleutian low that resulted in northeasterly winds along the Beaufort shelf and slope. Details regarding the atmospheric forcing of the storm, including regional effects due to the pack-ice and the orography of the North Slope of Alaska, can be found in Pickart et al. (2011).

The corresponding timeseries of alongcoast wind stress from the Barrow weather station is shown in Fig. 5. We have denoted three periods – pre-storm, height of the storm, and post-storm (Fig. 5) – and have constructed composite vertical sections for each of the three periods (Fig. 6). Before the onset of the strong winds (top panel of Fig. 6), the shelfbreak jet of Pacific Water was flowing to the east at $> 50 \text{ cm s}^{-1}$, with a deep “tail” of Atlantic Water also flowing to the east at $> 30 \text{ cm s}^{-1}$ (the white line in Fig. 6 denotes the water mass boundary between the Pacific and Atlantic water, as defined by Nikolopoulos et al., 2009). During the height of the storm the shelfbreak jet was reversed, flowing to the west at $> 70 \text{ cm s}^{-1}$, and Atlantic water was upwelled onto the shelf (middle panel of Fig. 6). It should be noted that the peak of the upwelling occurred roughly 18 h after the peak reversal of the jet, which is not captured in the composites shown here. Finally, after the cessation of the winds, a strong jet of Atlantic Water spun up ($> 50 \text{ cm s}^{-1}$, bottom panel of Fig. 6). Note also that the Pacific water shelfbreak jet was beginning to be re-established.

As explained in Pickart et al. (2011) using a numerical model, the development of the deep jet of Atlantic Water after the storm is the result of the adjustment of the sea surface height and density structure to the decrease in wind forcing. The sea surface height relaxes very quickly through barotropic wave propagation, while the density field in the water column adjusts through the

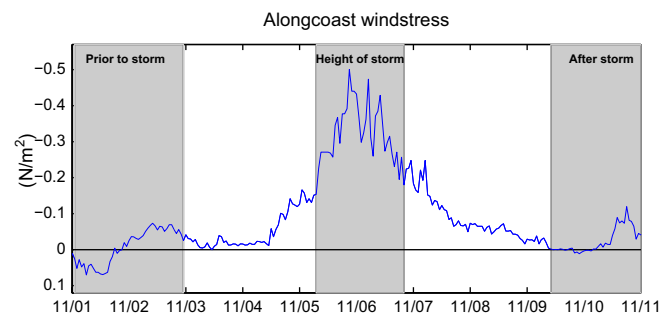


Fig. 5. Alongcoast wind stress at Barrow during early November 2002. The period of the three composite averages shown in Fig. 6 are indicated by the gray shading.

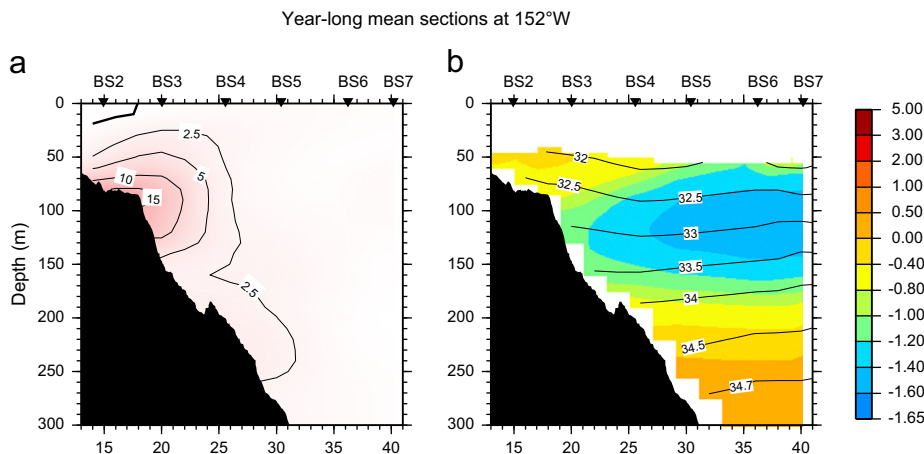


Fig. 4. Observed year-long mean vertical sections from the 152°W mooring array. (a) Alongstream velocity (cm s^{-1} , where positive is along 125°T). (b) Potential temperature (color, °C) with salinity (contours) overlaid. The means were computed over the time period 2 August 2002–31 July 2003 (from Nikolopoulos et al., 2009). (For interpretation of the references to color in this figure caption, the reader is referred to the web version of this article.)

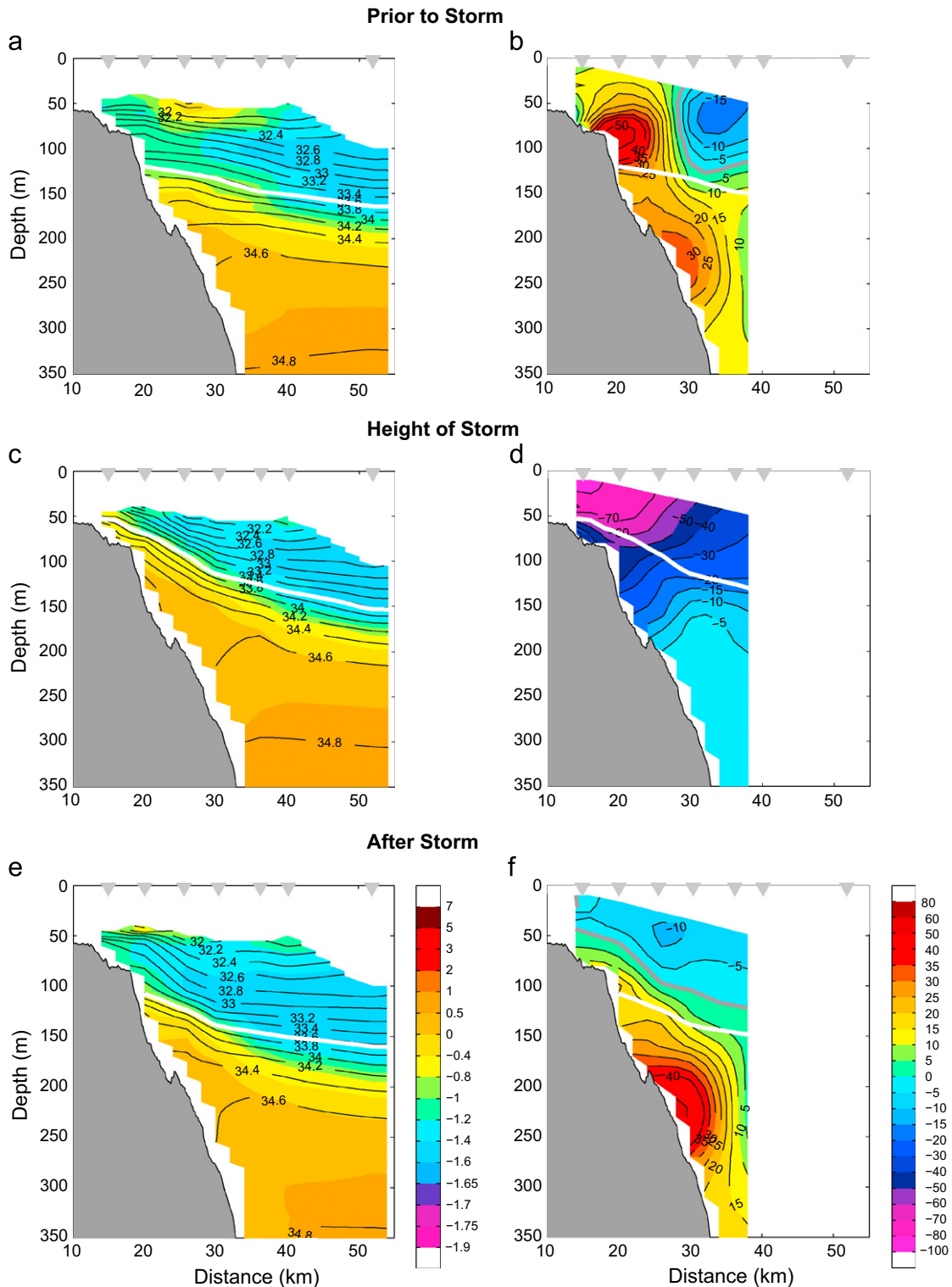


Fig. 6. Composite observed average fields before, during, and after the storm. The time period of the composites are shown in Fig. 5. The left-hand panels are potential temperature (color) overlain by salinity (contours). The right-hand panels are alongstream velocity, where positive is eastward (the thick gray line is the zero contour). The thick white line denotes the boundary between the Pacific water and Atlantic water (33.64 salinity contour, see Nikolopoulos et al., 2009). (For interpretation of the references to color in this figure caption, the reader is referred to the web version of this article.)

slower propagation of baroclinic waves. Because of the disparity in speeds between the barotropic and baroclinic adjustments, the westward wind-driven surface velocity of the upwelling jet quickly decreases, but the thermal wind shear stays nearly the same in the water column. Hence the subsurface velocity reverses to the east at depth, i.e. in the Atlantic Water. This deep jet spins

down at the baroclinic time scale (days to weeks), and was in fact spinning down from a previous event during the time period of the first composite in Fig. 6. The emergence of the deep Atlantic Water jet seems to be a ubiquitous feature of upwelling in the Alaskan Beaufort Sea (Nikolopoulos et al., 2009), and, since these events are so common, there is a signature of the deep eastward

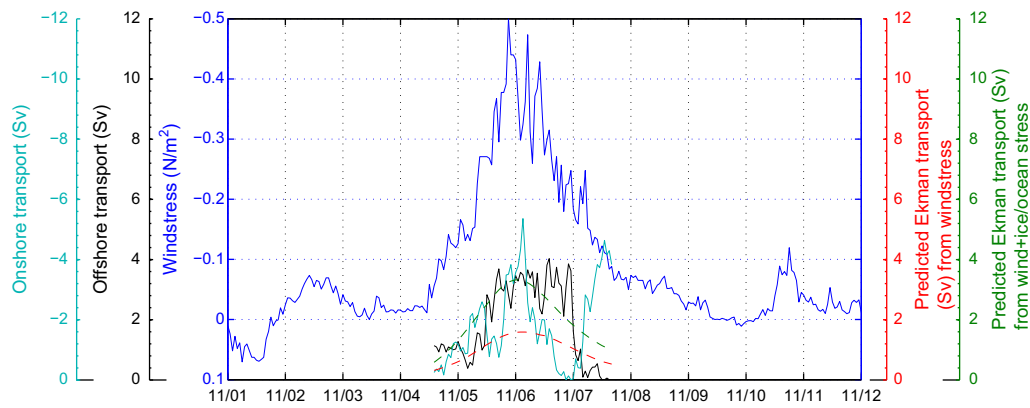


Fig. 7. Timeseries of the secondary circulation at mooring BS2 during the storm. The blue curve is the alongcoast wind stress at Barrow. The black curve is the measured offshore transport in the upper layer, and the cyan curve is the measured onshore flow in the lower layer. The low-passed predicted Ekman transport is shown for the wind stress (red dashed line) and for the combined wind and ice–ocean stress (green dashed line). (For interpretation of the references to color in this figure caption, the reader is referred to the web version of this article.)

flow in the year-long mean section of Fig. 4. For more details on the evolution of the alongstream flow during the November 2002 upwelling event, the reader is referred to Pickart et al. (2011).

3.2. Secondary circulation

During the storm an offshore flow developed in the surface layer and, in the vicinity of the shelfbreak, an onshore flow occurred at depth. The transport timeseries of these components of the secondary circulation at the edge of the shelf (mooring BS2) are shown in Fig. 7 over the period of strong winds, where the alongstream length scale of the storm is taken to be 500 km based on the National Centers for Environmental Prediction (NCEP) reanalysis fields. As the storm spins up and reaches its peak, the offshore and onshore flow generally track each other. However, as the winds subside (during the 24-h period from mid-day 6 November to mid-day 7 November) the wind-driven jet fluctuates such that the onshore flow at first weakens, followed by a weakening (strengthening) of the offshore (onshore) flow. When integrated over the full period of high winds, the two cross-stream flows roughly balance each other. Hence, there is little to no net mass flux across the shelfbreak associated with the storm. Note, however, that the cross-stream exchange is substantial, reaching more than 3 Sv at the peak of the storm. During the full duration of the storm a total of 350 km³ of water was exchanged between the shelf and the basin (over the 500 km length of the storm). To put this in perspective, this is equivalent to the volume of water flowing through Bering Strait over a period of 5 days (assuming an inflow of 0.8 Sv, Roach et al., 1995). The shelf–basin fluxes of various quantities during the storm are discussed in Section 5.

Generally speaking, observational estimates of the offshore surface-layer transport in upwelling systems tend to be consistent with the value predicted from Ekman theory (see Lentz and Chapman, 2004 for a review). The expression for the wind-driven Ekman transport is $(\tau_w L_x)/(\rho f)$, where τ_w is the alongcoast wind stress, ρ is the water density, f is the Coriolis parameter, and L_x is the alongstream length scale (taken as above to be 500 km). Using the 3-h lowpassed winds from the Barrow weather station to compute a smoothed version of the alongcoast wind stress in Fig. 5, and using the density at the shallowest measurement depth at mooring BS2 averaged over the upwelling event, we constructed a timeseries of the predicted offshore Ekman transport at the edge of the shelf, which is shown in Fig. 7 (dashed red curve). One sees that the measured offshore surface transport (and deep onshore flow) significantly exceeds the predicted value.

One possible explanation for this discrepancy is that the relative vorticity is large enough to make non-linear effects important. We estimated this by calculating the relative vorticity from the mooring data, and the effect was found to be minor.

Another possible reason for the difference between the wind-driven Ekman theory and our observed secondary circulation at the shelf edge is the presence of the pack-ice. When there is minimal internal ice stress (which is true for a partial ice cover that is “freely moving”) the transfer of stress from the atmosphere to the ocean is enhanced by the presence of ice. This is due to the irregular ice ridges and keels which lead to a more effective transfer of momentum (Pite et al., 1995). Williams et al. (2006) found that for upwelling winds in the Beaufort Sea the pack ice is quite mobile (seaward of the landfast ice), hence diminishing the impact of internal stress. We estimated the surface stress imparted to the water column due to the combination of wind and ice–ocean drag (see Yang, 2006)

$$\tau = \lambda \tau_{iw} + (1 - \lambda) \tau_w, \quad (2)$$

where $\tau_{iw} = \rho C_{iw} |\mathbf{u}_{ice} - \mathbf{u}_{ocean}| (\mathbf{u}_{ice} - \mathbf{u}_{ocean})$ is the ice–ocean stress, C_{iw} is the ice–water drag coefficient, and λ is the fractional ice cover. This says that the fraction of the water covered by pack-ice is driven by ice–ocean stress, while the remaining open water is forced directly by the wind stress. We take the surface water velocity \mathbf{u}_{ocean} in (2) to be the value extrapolated upwards to 5 m using the ADCP data at mooring BS2, which should be below the ice boundary layer, and the ice velocity \mathbf{u}_{ice} is that used by Pickart et al. (2009b) at the same location also measured by the ADCP.

During the storm, the ice concentration ranged from 50% to 70% (Fig. 8a), and it was advected strongly to the west (as fast as 1.5 m s⁻¹, Fig. 8b). One sees that the surface velocity tracked the ice velocity but was systematically weaker. Taking the value of the ice–water drag coefficient to be 0.0055 (Hibler, 1980), and using the ice-concentration timeseries together with the alongstream component of the ice–ocean stress, we computed the modified Ekman response (again the stresses were 3-h lowpassed and a 500 km alongstream length scale was assumed). As seen in Fig. 7, the predicted offshore transport (dashed green curve) is now more in line with the observations, suggesting that the enhanced secondary circulation observed during the storm was due to the mobile pack-ice imparting a larger surface stress to the water column. Hence, Ekman theory seems to apply to our observations when one takes into account the total surface stress.

The vertical structure of the secondary circulation during upwelling has been found to vary depending on conditions in the water column and on the geography of the location. A detailed

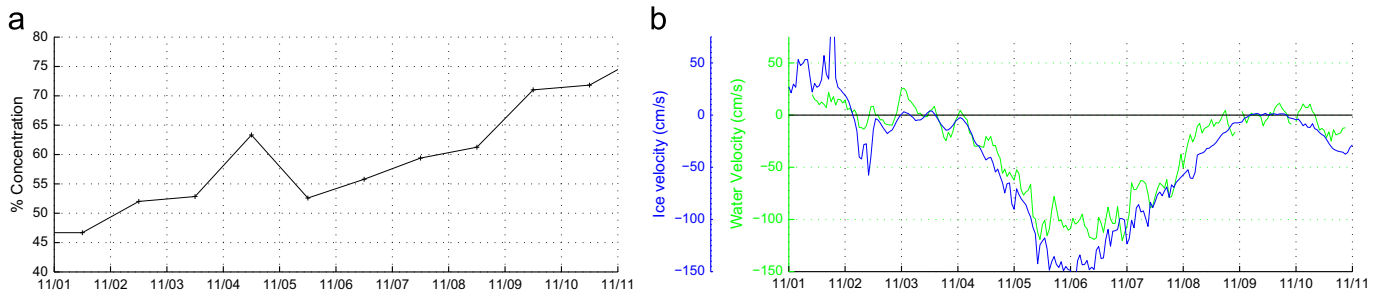


Fig. 8. (a) Ice concentration at the array site during the storm. (b) Measured alongstream velocity of the ice (blue) and water (extrapolated to 5 m depth, green) at mooring BS2 during the storm. The ice concentration and ice velocity timeseries are from Pickart et al. (2009b). (For interpretation of the references to color in this figure caption, the reader is referred to the web version of this article.)

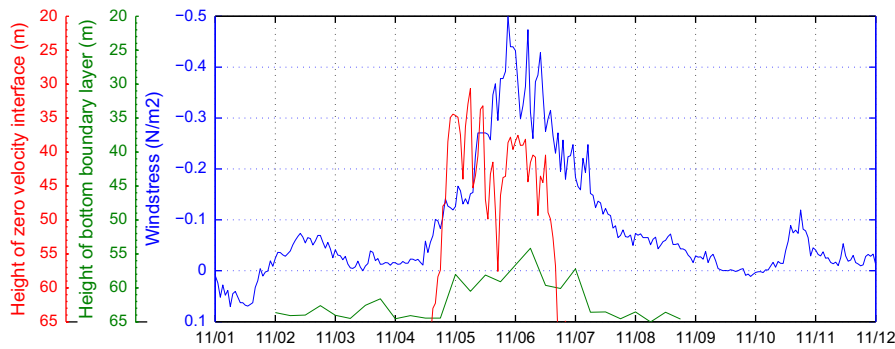


Fig. 9. Timeseries of alongcoast wind stress at Barrow (blue curve), height of the bottom boundary layer at mooring BS2 (green curve), and the height of the zero cross-stream velocity interface at mooring BS2 (red curve) during the storm. (For interpretation of the references to color in this figure caption, the reader is referred to the web version of this article.)

summary is provided by Lentz and Chapman (2004) who show that the onshore flow at depth is sometimes confined to the bottom boundary layer, while in other instances it is distributed more throughout the water column. The former is true when the surface stress tends to balance the bottom stress. As discussed in Lentz and Chapman (2004), the pertinent non-dimensional parameter is the slope Burger number $B = \alpha N / f$, where N is the buoyancy frequency and α is the bottom slope. The Burger number is a measure of the vertical penetration scale relative to the depth of the water column. When $B \ll 1$ the surface and bottom stress balance one another and the return flow is contained within the bottom boundary layer. In contrast, when B is $O(1)$ or larger, the return flow spans more of the water column. We estimated B during the time period of the storm at each of the mooring sites using the moored profiler data to calculate N , and a smoothed version of the cross-stream bathymetric profile (obtained from the ship's echosounder) to calculate the bottom slope. At the BS2 mooring site on the outer shelf, $B \sim 0.7$ which suggests that the return flow should not be confined to the bottom boundary layer (B was even larger farther offshore). It also implies that the alongstream momentum balance during the storm should involve more than just the surface stress and bottom stress, which is indeed the case (see Section 4 below).

The fact that the moorings were equipped with CTD profilers, providing continuous traces of temperature and salinity, allowed us to identify and investigate the characteristics of the bottom boundary layer. Following the procedure used in Pickart et al. (2002), we objectively determined the height of the bottom boundary layer at each time step through the storm and tabulated the vertically averaged properties of the layer. During the storm, at the edge of the shelf, the bottom boundary layer became warmer and saltier as the upwelling commenced, and also became more weakly stratified (except at the end of the storm when the stratification increased

abruptly). The evolution of the height of the bottom boundary layer at mooring BS2 is shown in Fig. 9 (green curve). One sees that the height of the layer increased by roughly 10 m during the storm to a maximum of 25 m above the bottom (the bottom depth at the mooring site was 80 m). Was the return flow confined to the bottom boundary layer? As noted above, the secondary circulation at the shelf edge was offshore at shallow depths and onshore deeper in the water column. Using the cross-stream velocity record from the ADCP at mooring BS2 we tabulated the height of the zero crossing, which is shown as well in Fig. 9 (red curve). In general, the velocity interface height is 15–20 m shallower than the bottom boundary layer height. This indicates that the return flow was not confined to the bottom boundary layer, consistent with the calculated Burger number and the results presented in Lentz and Chapman (2004).

4. Alongstream momentum balance

4.1. Observations

The above results demonstrate that, for the storm in question, the secondary circulation at the edge of the shelf is consistent with a two-dimensional Ekman cell where the off-shelf flow in the surface layer is compensated by the return flow at depth. In an analysis of the full suite of 45 upwelling events over the two-year SBI period, Schulze and Pickart (2012) showed that such a balance is generally achieved. That is, there is little to no net wind-driven mass flux across the shelfbreak during these storms. The fact that B is $O(1)$ at this location suggests further that the surface stress is not balanced by the bottom stress. To investigate the alongstream force balance, we evaluated the depth-integrated alongstream momentum equation over the course of the storm. This was done using the gridded vertical sections to compute the

pertinent quantities and cross-stream gradients at a cross-stream distance of 18 km, which is between moorings BS2 and BS3 near the shelfbreak (Fig. 2). (We note that using the original mooring data at these two sites leads to similar results.)

Vertically integrating over the water column, the alongstream momentum balance is

$$\frac{\partial}{\partial t} \int_{-h}^0 u \, dz = \left[\frac{\tau_x}{\rho_o} - \frac{\tau_{bx}}{\rho_o} - \frac{\partial}{\partial y} \int_{-h}^0 (uv) \, dz + f \int_{-h}^0 v \, dz - \frac{1}{\rho_o} \int_{-h}^0 \frac{\partial p}{\partial x} \, dz - \frac{\partial}{\partial x} \int_{-h}^0 u^2 \, dz \right], \quad (3)$$

where x, y are the alongstream and cross-stream directions, u, v are the corresponding velocity components, z is the vertical direction, τ_x is the alongstream component of the surface stress as discussed above (i.e. the combined wind + ice/ocean stress), τ_{bx} is the alongstream component of the bottom stress, p is the pressure, ρ_o is the average density (averaged vertically and in time), and h is the height of the water column. For the bottom stress we used the expression $\tau_b = C_d \mathbf{u}_{bot} |\mathbf{u}_{bot}|$, where \mathbf{u}_{bot} is the velocity at the deepest ADCP bin and C_d is the drag coefficient, taken here to be 1.5×10^{-3} (J. Trowbridge, personal comm., 2012).

The left hand side of (3) is the local acceleration of the vertically averaged alongstream velocity near the shelfbreak, and the terms on the right hand side are the contributing forces: the surface stress, bottom stress, divergence of cross-stream momentum flux, Coriolis force, alongstream pressure gradient, and the divergence of alongstream momentum flux. Assuming that the alongstream gradient of u is small, the last term can be ignored and is not considered further in the paper. We are interested in determining what factors caused the shelfbreak jet to reverse to the west during the storm and, as the winds subsided, what caused it to become re-established to the east. Accordingly, we evaluated each of the remaining terms in (3) over the length of the storm. We note that the pressure gradient term cannot be measured directly, and so it is computed as a residual. As discussed in Lentz and Chapman (2004), since B is $O(1)$ we

would expect the non-linear cross-stream divergence term to be an important part of the momentum balance.

Before presenting the results, we implemented a further simplification as follows. Through most of the period of strong winds the Coriolis term was small, but, as discussed in Pickart et al. (2011), near the end of the storm there was a strong onshore component to the flow at all of the mooring sites. During this time the residual in (3) is large and approximately balances the large Coriolis force. We interpret this as a geostrophically balanced onshore flow that occurred near the end of the storm, perhaps the front end of an anticyclonic eddy which are common in this region (e.g. Spall et al., 2008). As such, we discounted the Coriolis term from the momentum balance. This in effect makes the pressure gradient term (the residual) reflect the ageostrophic pressure gradient only. It has no effect for most of the storm, but serves to remove the eddy-like feature at the end. It also affords for a more meaningful comparison to the model momentum balance presented in Section 4.2 (which contains no such eddy).

The timeseries of the remaining terms on the right hand side of (3) are displayed in Fig. 10. In addition, we show the vertically averaged alongstream velocity (thick dashed black curve) and the alongstream acceleration (thick red curve, which is the left hand side of Eq. (3)). In the figure, negative values act to accelerate the upwelling jet westward, and positive values act to decelerate it (i.e. re-establish the normal eastward-flowing shelfbreak current). Note that prior to the storm and after the storm, when the reversed jet is absent, all of the momentum terms are close to zero and the measured quantities essentially balance each other (i.e. the residual is small). This gives us confidence that the mooring data are providing a realistic and accurate assessment of the force balance.

What factors act to spin up and then spin down the upwelling jet? First consider the two stress terms. The surface stress (blue curve) accelerates the jet westward, while the bottom stress (magenta curve) acts to retard it. These two terms are nearly in phase with each other because the reversed jet lags the wind

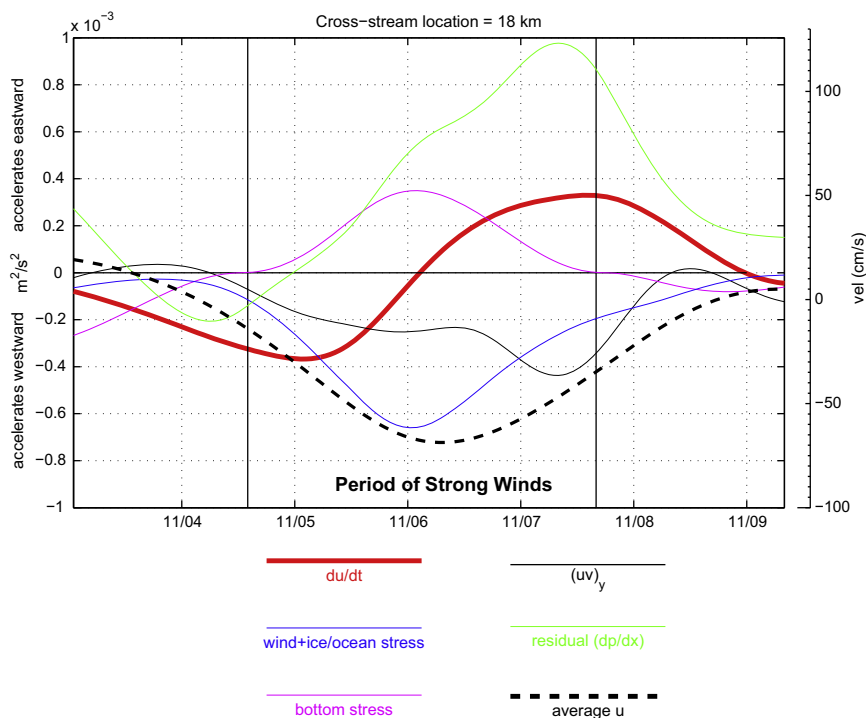


Fig. 10. Terms in the vertically averaged alongstream momentum balance calculated from the observations. The different terms are listed in the key and explained in the text.

only slightly. However, they do not balance each other, which is consistent with the relatively large value of the Burger number as discussed above. The next term is the divergence of cross-stream momentum flux (black curve) which also acts to accelerate the jet westward throughout the storm at this location. The sign of this term was not obvious a-priori, and in fact is opposite to that of the momentum flux divergence term in the theoretical model of Lentz and Chapman (2004). Consequently, this implies that the alongstream pressure gradient is primarily responsible for spinning down the upwelling jet—even before the winds subside. In particular, the pressure gradient (green curve) increases through the storm, and subsequently diminishes after the storm ends. This is understandable in that, in the vicinity of the array, the sea surface height decreases due to the offshore Ekman transport, while to the west – either outside the area of direct storm influence or beyond Pt. Barrow where the coastline turns to the south – the sea surface height remains relatively undisturbed. This change in sea surface height could then account for the alongstream pressure gradient deduced from (3).

It is of interest to consider more carefully the nature of the momentum flux divergence in order to understand why it acts to accelerate the upwelling jet near the shelfbreak, in contrast to the results of Lentz and Chapman (2004). In the Lentz and Chapman (2004) theoretical model, which is steady in time, the thermal wind shear of the alongstream (upwelling) jet is assumed constant throughout the domain. At a given location there is a net cross-stream flux of alongstream momentum because the surface Ekman flow advects strong alongstream velocity offshore, while the return flow at depth advects weaker alongstream velocity onshore. The reason why there is a divergence in momentum flux is that, as one progresses offshore into deeper water, the deep return flow advects even weaker alongstream velocity onshore. This divergence results in a deceleration of the depth-mean alongstream jet. The critical factors in this case are the change in bottom depth (getting deeper offshore) in conjunction with the thermal wind shear.

In contrast, in our observations the important factors are a combination of the change in the strength of the secondary circulation and a change in structure of the alongstream flow as one progresses offshore. Unlike the Lentz and Chapman (2004) model, the change in bottom depth does not play a significant role here. In particular, the secondary circulation weakens seaward of the shelfbreak (see Pickart et al., 2011), and the lateral position of the maximum alongstream flow varies with depth. These aspects of the circulation are shown schematically in Fig. 11. Progressing from mooring BS2 to BS3, the cross-stream flow decreases (indicated by the flow vectors in the schematic); at the same time, the alongstream flow in the upper layer decreases, while the alongstream flow at depth increases (indicated by the shading in the schematic). This structure of the primary flow is likely due to the fact that the stratification – and hence the thermal wind shear – is not constant throughout the water column. The stratification is strongest in the halocline, and during the upwelling process the halocline shoals towards the shelf (Fig. 6c). This in turn implies that the thermal wind shear is greater at the BS2 site than it is at the BS3 site (although this can't be checked because the profilers did not extend into the upper part of the water column). Consequently, the flow would decrease more rapidly with depth at BS2, which could account for the variation in alongstream velocity seen in the observations and shown schematically in Fig. 11.

The impact on the cross-stream divergence of momentum flux due to both of these factors – the weakening of the secondary flow and the structural change of the primary flow – is elucidated as follows. Two calculations were carried out. In the first, we used the full alongstream velocity fields but laterally averaged the

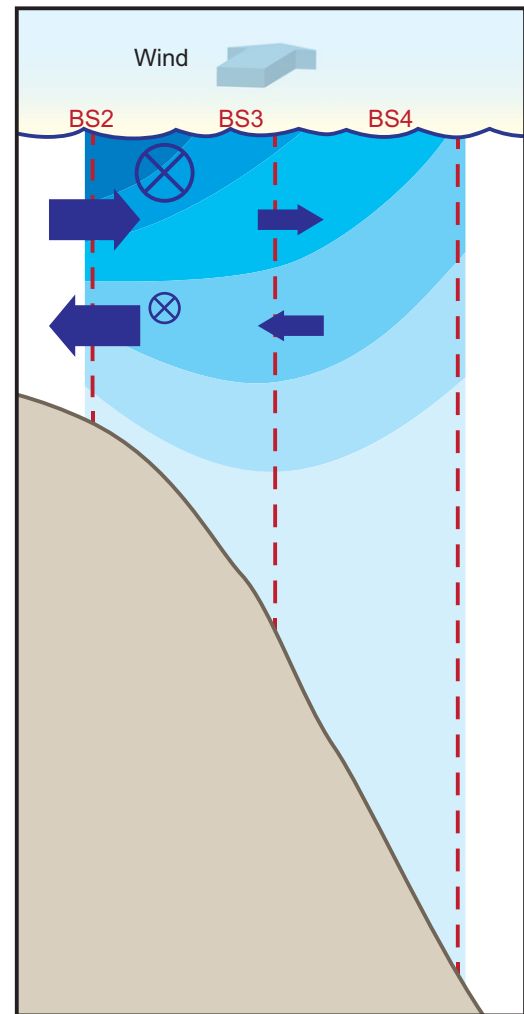


Fig. 11. Schematic of the primary flow (blue shading) and secondary flow (vectors) during the storm. Mooring locations are indicated schematically as well. (For interpretation of the references to color in this figure caption, the reader is referred to the web version of this article.)

secondary flow at each depth for each time step. This served to isolate the effect of the cross-stream variation in the primary flow (Fig. 11). We limited the vertical domain of the calculation to the depth of the BS2 mooring, which served to remove the varying bottom depth from consideration. This produced a timeseries of momentum flux divergence similar to that seen in Fig. 10. In the second calculation we laterally averaged the alongstream flow at each time step, while using the observed cross-stream flow fields. This isolated the impact of the weakened secondary circulation offshore of the shelf. Again, the resulting timeseries was similar to that obtained using the full fields of the two velocity components. In both instances the magnitude of the momentum flux divergence was comparable. This demonstrates that both of the factors noted above are important in contributing to the non-linear momentum term that helps drive the westward jet in the vicinity of the shelfbreak.

Detailed inspection of the evolution of the storm reveals that there are two regimes – one as the storm spins up and the other as it spins down – that result in the negative momentum flux divergence. (The schematic of Fig. 11 reflects primarily the spin-up phase.) For simplicity let us consider only the spin up phase in order to provide further intuition regarding the non-linear acceleration of the upwelling jet. For the first calculation above, in the upper layer, faster westward velocity is advected offshore from

the shelf while slower westward velocity is advected in the same direction seaward of this. This accumulates westward momentum in the upper layer. By contrast, in the lower layer, faster velocity is advected from offshore while slower velocity is advected onto the shelf. Again this results in an accumulation of westward momentum, so the net effect is an acceleration of the depth-integrated upwelling jet. For the second calculation above, the offshore flow in the upper layer is convergent, resulting in an accumulation of westward momentum, while the onshore flow at depth is divergent leading to a deficit of westward momentum. However, the alongstream flow is weaker at depth, so the convergence in the upper layer dominates and again the net effect is to accelerate the depth-integrated upwelling jet. These arguments demonstrate that the detailed structure of both the primary and secondary circulation is fundamentally important in determining the sense of non-linear momentum forcing during upwelling in the Alaskan Beaufort Sea. For the storm in question, in the vicinity of the shelf-edge, this force acted in concert with the surface stress to reverse the normally eastward-flowing shelfbreak current and drive a very strong westward-flowing upwelling jet exceeding 1 m s^{-1} at its peak.

4.2. Model

The numerical model used in this study (described in Section 2.3) was also employed by Pickart et al. (2011) to investigate some of the aspects of the November 2002 storm, including the cause of the deep flow of Atlantic water near the end of the storm. Here we briefly review the basic wind-driven response in the model, then use the model fields to evaluate the depth-integrated momentum budget to compare with the observational results above. The general oceanic response is demonstrated in Fig. 12 by vertical sections of salinity, zonal velocity, and meridional velocity at 1000 km longitude on day 3 (see Fig. 3). The easterly wind forces an offshore Ekman transport in the upper layer (Fig. 12d),

which induces upwelling along the coast. The meridional velocity is dominated by the offshore Ekman transport in the upper layer and the onshore transport at depth (Fig. 12d). This brings water from offshore and below the shelfbreak up onto the shelf (Fig. 12b). The surface salinity is a maximum over the shelf (approximately 20 km latitude) and in the region of strongest winds (near 1000 km longitude). This is because upwelling has brought salty water onto the shelf, and vertical mixing entrains this water into the surface mixed layer (Fig. 12b). This region of local maximum in salinity propagates slowly eastward during the model run. The offshore transport also results in a reduced sea surface height near the coast, which drives a westward along-shelf current (Fig. 12c). The upwelled dense water reduces the offshore pressure gradient with depth, resulting in vertical shear in the alongshore velocity.

The terms in the zonal momentum equation have been calculated from the model integration at 1000 km longitude and 28 km latitude (indicated by the white line in Fig. 12). This location is representative of the balances all along the region of strong wind forcing, although the magnitude and timing varies, as shown below. For ease of comparison, the presentation of the model momentum terms in Fig. 13 is the same as in Fig. 10 for the observations. Overall, the model tendencies and influences of each of the momentum terms are very similar to what was diagnosed from the observations. The surface stress is negative throughout, forcing the zonal velocity towards the west (Fig. 13, blue line). The zonal flow spins up over the first 2–3 days, then begins to decelerate (black dashed line). This decrease in the strength of the westward flow occurs even as the wind is still forcing the flow to accelerate towards the west. The time rate of change of the zonal velocity changes sign at roughly 2.5 days, well before the wind forcing ceases (red line). As implied by the observations, this is primarily due to the ageostrophic zonal pressure gradient (pressure term plus the Coriolis term, green line). The bottom stress (magenta line) is also opposing the

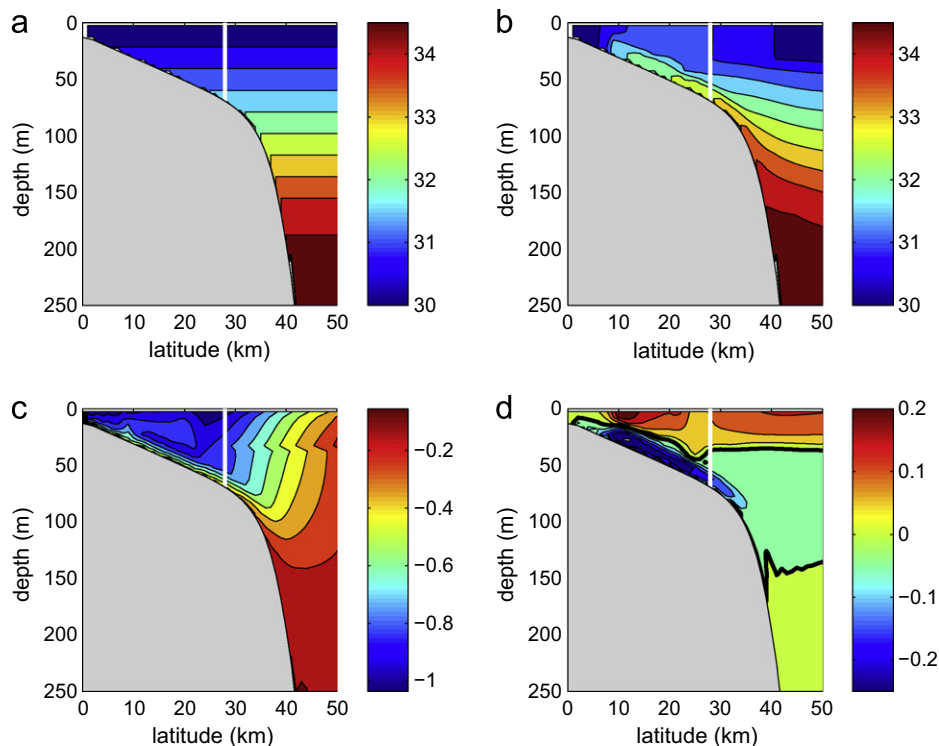


Fig. 12. Vertical sections from the numerical model at 1000 km longitude. (a) Initial salinity (contour interval 0.5), (b) salinity on day 3 (contour interval 0.5), (c) zonal velocity on day 3 (contour interval 0.1 m s^{-1}), and (d) meridional velocity on day 3 (contour interval 0.05 m s^{-1}). The thick black line is the zero contour. The white line in each panel denotes where the model momentum balance was evaluated.

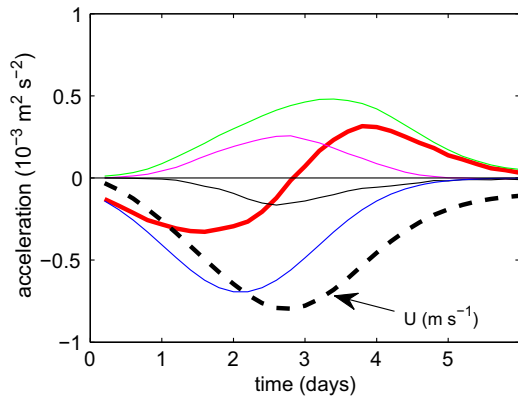


Fig. 13. Depth integrated terms in the zonal momentum equation at $x=1000$ km and $y=28$ km from the numerical model, to be compared to Fig. 10 from the observations. Red: time rate of change; blue: wind stress; green: pressure gradient plus Coriolis; black: non-linear advection; magenta: friction; and black dashed: zonal velocity. (For interpretation of the references to color in this figure caption, the reader is referred to the web version of this article.)

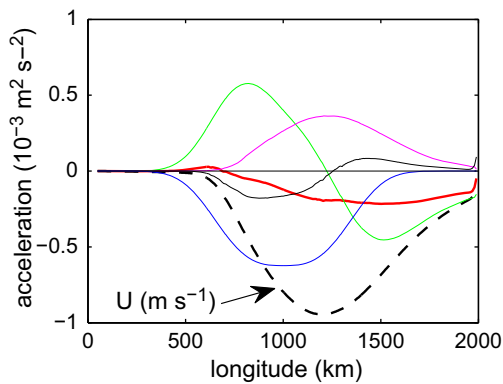


Fig. 14. Depth integrated terms in the zonal momentum budget from the numerical model on day 3 at $y=28$ km, as a function of longitude. Red: time rate of change; blue: wind stress; green: pressure gradient plus Coriolis; black: non-linear advection; magenta: friction; and black dashed: zonal velocity. (For interpretation of the references to color in this figure caption, the reader is referred to the web version of this article.)

westward acceleration, although it is consistently weaker than both the surface stress and the pressure gradient term. The non-linear advection term is tending to accelerate the flow towards the west, as in the observations, although it is somewhat smaller in magnitude (black line).

The model suggests that the balance of terms in the zonal momentum equation varies significantly with longitude. The depth integrated contribution for each of the terms as a function of longitude (at 28 km latitude) on day 3 is shown in Fig. 14. The zonal flow is weak in the western part of the domain compared to the eastern part, even though the forcing is symmetric about longitude 1000 km. This is a result of the eastward propagation of the pressure field, which accelerates the flow towards the east in the western part of the domain and towards the west in the eastern part of the domain (green curve). At this time the pressure contribution dominates in the western forcing region, approximately balancing the wind term. In the center of the forcing region, both bottom friction and the non-linear term become important as well. In the eastern region, the pressure gradient term changes sign, accelerating the flow towards the west. This is where the sea surface height returns to its unperturbed value. Bottom stress is very important in the eastern region as well, where the zonal velocity is the strongest. This general pattern of the force balance propagates towards the east in time.

5. Cross-stream fluxes

As presented above, there is little to no net flux of mass across the shelfbreak during the storm in question, which seems to be the case for most of the upwelling storms in the Alaskan Beaufort Sea (Schulze and Pickart, 2012). However, because of the layering of the different Pacific and Atlantic water masses through the water column, there is indeed a net flux of various properties such as heat, salt, and nitrate. We now use the timeseries of the hydrographic and cross-stream velocity profiles at the shelf edge (mooring BS2), along with water sample data of chemical properties collected in the vicinity of the array, to estimate some of these fluxes for the November 2002 storm. Recall, however, that the hydrographic profiles extend only to 45 m depth, and the chemical data were collected only during the cruises to service the moorings. Hence, we need to make some assumptions in order to derive the flux estimates.

5.1. Heat and salt fluxes

5.1.1. Methodology

Two assumptions are made in order to construct salinity and temperature data in the upper layer. The first is that the water that gets upwelled shoreward of the inshore mooring in the lower layer (which is measured by the moored profiler) immediately gets fluxed offshore in the upper layer. This is akin to assuming that the shelf is narrow. This assumption would tend to cause an underestimate of the fluxes, since the surface water on the shelf that actually gets fluxed offshore (at least initially) is more anomalous in its properties. In particular, the water is warmer and fresher than the water getting upwelled. The second assumption is that once the upwelled water passes beyond the region of measurement (i.e. past the top float of the mooring) it maintains its vertical structure. We take this vertical structure to be a mean representation (explained shortly) of the water drawn from depth that gets advected past the moored profiler. This approach is made possible because, in the three weeks prior to the upwelling event, ambient boundary current water resided offshore and deeper than mooring BS2. During this time – before the onset of the strong winds – the isopycnals slowly migrated upward, allowing the moored profiler to sample this ambient water.

The calculation of the representative water column structure drawn from depth was carried out as follows. The measured hydrographic profile at mooring BS2 three weeks before the upwelling event (on October 10) was taken to be the initial mean profile (which of course spanned only the water column below 45 m). At the next measurement period 6 hours later, at which point the isohalines were displaced slightly shallower, the second profile was adjusted vertically so that the region of common measured salinities between the two profiles matched in a least squares sense. The average of this combined profile was taken as the next mean profile, which now spanned a bit more than 45 m. This procedure was carried out iteratively for the full three week period plus that of the storm. For potential temperature we applied the same vertical adjustments computed above to the instantaneous temperature profiles (which were not monotonic) at each time step to arrive at an analogous result. The final mean profiles of temperature and salinity are shown in Fig. 15 (thick lines), where the means are positioned vertically so that the value of salinity at 45 m depth is equal to that of the minimum measured salinity at that depth during the storm. The gray symbols in the figure are the individual measurements that comprised the iterative calculation. There are two important aspects to note in the figure. The first is that, although there is significant scatter, a clear vertical structure is present for each property which is a realistic reflection of the water masses. In

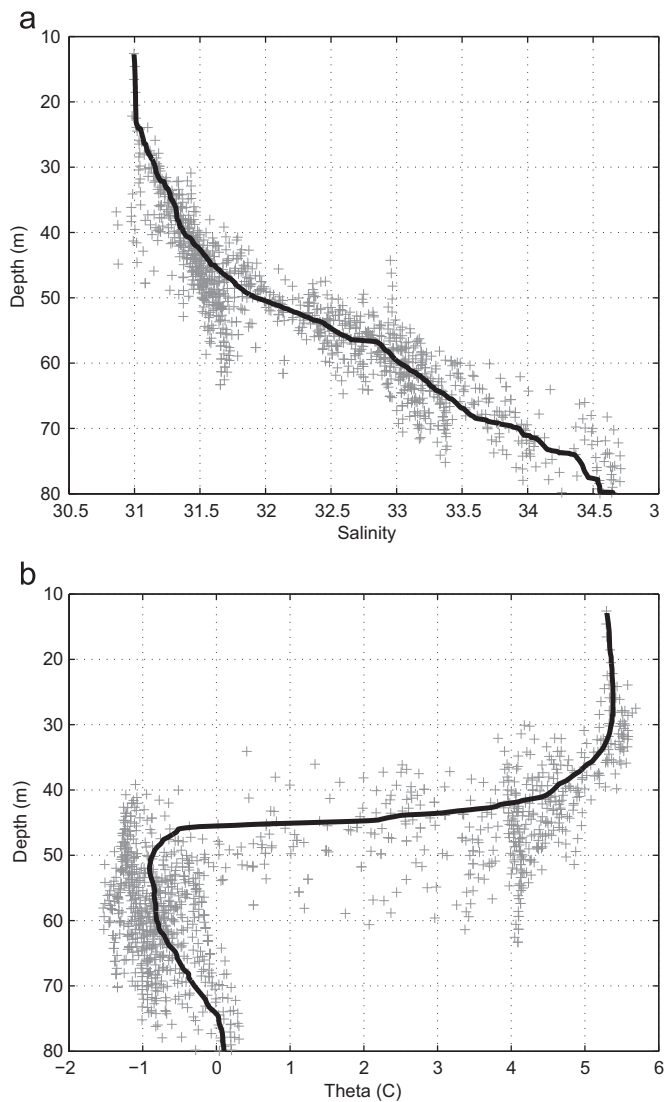


Fig. 15. Constructed vertical profiles for inferring the upper layer data (see text for explanation). The solid lines are the mean profiles and the gray symbols are the original data. (a) Salinity and (b) potential temperature ($^{\circ}\text{C}$).

particular, near the surface one sees warm, fresh Alaskan Coastal Water (warmer than 5°C and as fresh as 31). Below this resides the remnant Pacific Winter Water (near -1°C , 32.5), and a thin layer of Atlantic Water is found near the bottom (greater than 0°C and 34.25). The second thing to note in Fig. 15 is that the data extend to approximately 10 m depth. This means that most of the water column is covered, even at the start of the upwelling event.

To complete the construction of full-depth hydrographic profiles during the storm, the following procedure was implemented. At each time step the value of salinity at 45 m as measured by the moored profiler was documented, and the portion of the mean profile fresher (shallower) than this was appended to the measured profile. The same was done for temperature. As such, we used the actual measurements where they existed and the synthesized measurements shallower than this. The overall property flux for the storm is the product of the time-averaged hydrographic and cross-stream velocity profiles over the duration of the storm. Since there are no ADCP measurements or hydrographic profile data (even the synthesized product) in the upper 10 m and bottom 10 m, we extrapolated into these regions. This was done using constant curvature, except for the shallow

portions of the hydrographic profiles which were assumed constant over the top 10 m. Finally, after the mean velocity was extrapolated as such, we adjusted this profile with a small barotropic offset (0.7 cm s^{-1}) to exactly balance mass. This allows for a clean interpretation of the cross-stream fluxes (e.g. Pickart and Spall, 2007; Tsubouchi et al., 2012).

5.1.2. Heat flux

The resulting mean profiles of cross-stream volume flux per unit depth and heat flux per unit depth, along with their vertical integrals, are shown in Fig. 16a and b. We note again that the alongstream length scale of the storm was approximately 500 km, which is incorporated into Fig. 16 and into our flux calculations. This distance is also roughly the length of the Alaskan Beaufort shelf. Hence, we interpret our estimated fluxes as representative of the entire shelf edge for a single autumn storm. One sees that even though mass is balanced, the heat flux is not. That is, more heat is fluxed offshore than onshore (the vertical integral is positive). We note that the net heat flux computed here is independent of reference temperature due to the fact that the mass is balanced (the reference temperature in Fig. 16b is 0°C). The strength of the overturning cell was 1.3 Sv (Fig. 16a, blue curve), and the relevant time scale of the storm is 73 h or roughly three days (i.e. the period during which the secondary flow was active, Fig. 7). This implies that a total of 350 km^3 of water was exchanged across the shelfbreak during the storm. The approximate volume of the Alaskan Beaufort shelf is 1500 km^3 , which suggests that the shelf could be completely replenished by 4–5 such storms. During the month of November 2002 there were in fact three upwelling storms.

Note that three different water masses participated in the event—very warm Alaskan Coastal Water in the upper layer, cold remnant winter Pacific Water below this, and moderately warm Atlantic Water at depth.³ The net result was an off-shelf heat flux of 29 TW (Fig. 16b, blue curve), which, when integrated over the length of the storm, resulted in $7.6 \times 10^{18}\text{ J}$ of heat being transferred to the basin. How important is this quantity? For comparison, Woodgate et al. (2006) calculated that roughly $3.5 \times 10^{20}\text{ J}$ of heat passed through Bering Strait over the course of a year during the early 2000s (i.e. during the period of the SBI mooring program). However, Woodgate et al.'s (2006) value was not an absolute heat flux, but rather the amount of heat, relative to the freezing point of sea water, available for melting ice. The equivalent quantity for our storm, integrated over the offshore-directed flow in the upper layer, is $9.8 \times 10^{18}\text{ J}$. This suggests that the amount of heat fluxed into the Canada Basin during the storm in question was comparable to 2.8% of the heat advected through Bering Strait in a year.

There are several caveats to consider with the above calculation and the comparison to Bering Strait. One must keep in mind that only a relatively small portion of the Bering Strait transport ends up on the Beaufort shelf and slope. Using the high-resolution SBI mooring array data, Nikolopoulos et al. (2009) calculated a mean eastward transport of Pacific water of 0.13 Sv, which is only 16% of the long-term Bering Strait average (0.8 Sv, Roach et al., 1995). Furthermore, mooring BS2 is on the inshore side of the shelfbreak jet, which excludes a good portion of the Bering Strait origin water from our calculation (keep in mind that we are estimating the off-shelf flux). In the second year of the SBI field program a mooring was maintained inshore of BS2. Using those data we estimate that roughly 20% of the boundary current resides near or inshore of the shelf edge. Consequently, this

³ The upwelled Atlantic water only reached the shelf edge near the end of the event and thus had minimal impact on the overall heat flux.

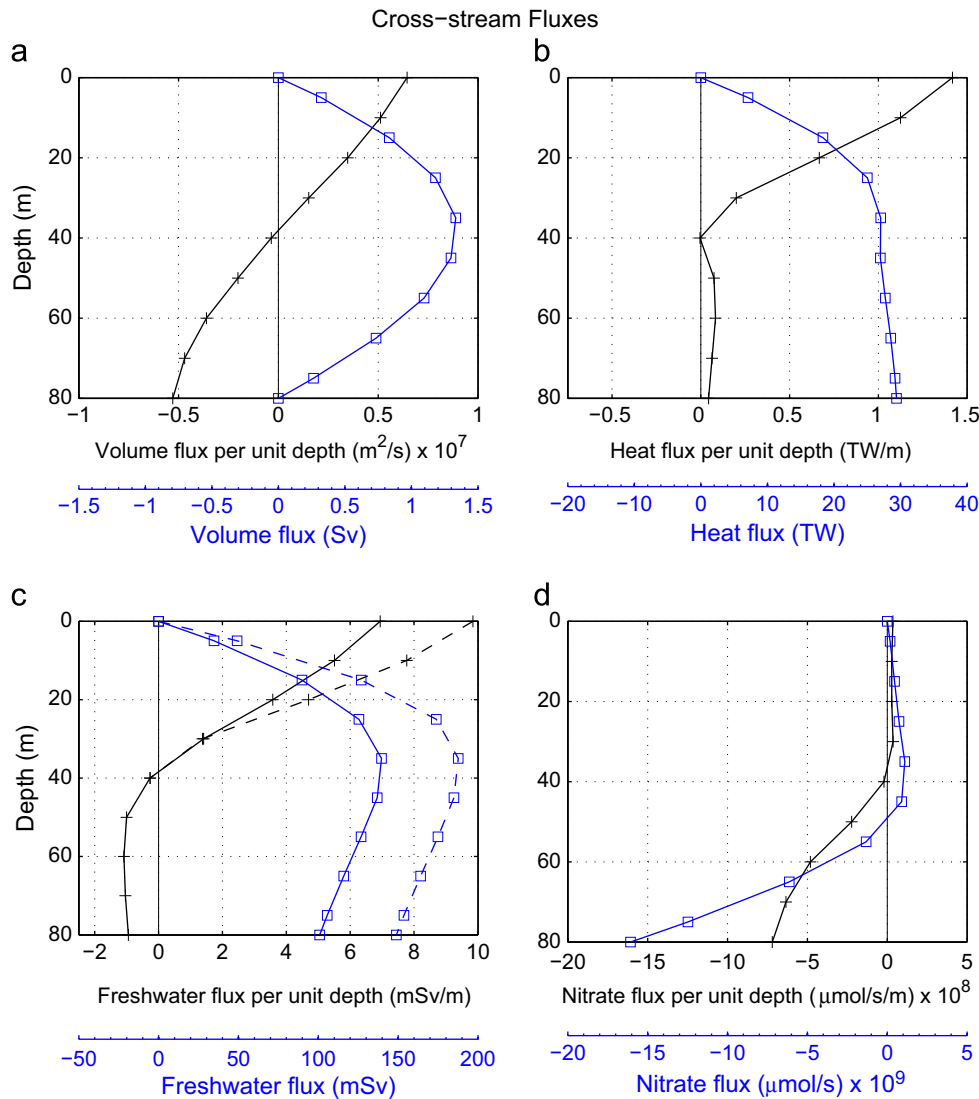


Fig. 16. (a) Vertical profile of cross-stream volume flux per unit depth at the edge of the shelf averaged over the storm (solid black line) and the vertical integral (solid blue line) which represents the cumulative transport as a function of depth. The transport was computed using $\Delta z=5$ m for the surface and bottom grid points, and $\Delta z=10$ m for the remaining grid points. (b) Profile of average heat flux per unit depth (solid black line) and the vertical integral (solid blue line). The reference temperature is 0°C . (c) Profile of freshwater flux per unit depth relative to 34.8 (solid black line) and the vertical integral (solid blue line). The dashed curves use the winched profiler data in the upper layer (see text). (d) Profile of average nitrate flux per unit depth (solid black line) and the vertical integral (solid blue line). (For interpretation of the references to color in this figure caption, the reader is referred to the web version of this article.)

would suggest that the storm in question was capable of fluxing nearly all of the yearly inventory of Pacific-origin heat from the Beaufort shelf.

The reader is reminded that the November 2002 storm was strong, and, as presented above, the offshore Ekman flux was enhanced by the presence of the partial ice cover. In addition, we have assumed that the warm Alaskan Coastal Water was present throughout the length of the Alaskan Beaufort Sea, which may not be the case. This implies that our estimate may not be representative. However, in each of the SBI years, five upwelling storms occurred from late-summer to mid-fall (when Alaskan Coastal Water should be present), implying that the cumulative effect of such storms is indeed substantial. It is also worth noting that the heat fluxed offshore during the storm may not have been entirely of Pacific origin; local heating on the shelf during the late-summer likely warmed the resident shelf water. Regardless of its origin, however, the off-shelf flux of heat would be available for melting $32,000\text{ km}^2$ of 1 m thick ice in the basin, which is equivalent to an area the size of the Beaufort shelf. Finally,

it should be noted that downwelling events, with a secondary circulation in the opposite sense, will tend to offset the cross-stream fluxes that arise from the upwelling storms. However, downwelling occurs less frequently in this region (there were less than half as many downwelling storms as upwelling storms during the SBI period). Also, the mixing that occurs during upwelling events makes them, to some extent, irreversible.

5.1.3. Salt flux

The net on-shelf flux of salt during the storm was 9.9×10^{11} kg (the result of fresher water advected seaward and saltier water advected shoreward). This can be put into perspective by noting that a 5-day polynya event on the Chukchi shelf injected 5×10^{11} kg of salt into the water column (Weingartner et al., 1998). Thus, the two phenomena can be of similar order in terms of supplying salt to the shelf. With regard to freshwater, following earlier studies we use a reference salinity of 34.8 (see Sutherland and Pickart, 2008). The resulting mean vertical profile of freshwater flux per unit depth and

its vertical integral are shown Fig. 16c (solid curves). The total volume of freshwater fluxed offshore during the storm was 26 km^3 , but for comparison to Bering Strait we use the value fluxed seaward in the upper layer (as was done above for the heat flux), which is 37 km^3 . From Woodgate et al. (2006) the annual amount of freshwater progressing through Bering Strait at the time of the SBI program was roughly 1800 km^3 . This implies that the storm fluxed an amount of freshwater equivalent to 2.0% of the annual delivery into the Arctic. This suggests a comparable degree of off-shelf permeability for freshwater as for heat.

As mentioned above, the assumption of a narrow shelf in our flux calculation likely resulted in an underestimate of the true freshwater flux, because less salty water resides (at least initially) in the surface layer as one progresses shoreward on the shelf due to the presence of the Alaskan Coastal Water. In an effort to address this we used data obtained from a winched profiling device that was attached to the top float of mooring BS3 in 2005 (the year after the SBI program). The device, which contained a CTD, profiled the water column above the top float from 45 m to 10 m. We computed the average salinity profile during the time of strong upwelling in the fall, and appended this to the mean salinity profile of the storm in question (i.e. replacing the synthesized data in the upper layer). Even though the two profiles were obtained at different cross-stream locations (separated by 5 km) and in different years, they matched perfectly at the depth of the top float, giving one confidence that this was a meaningful exercise. The revised off-shelf freshwater flux per unit depth and the vertical integral are shown by the dashed curves in Fig. 16c. This increases our net flux estimate for the storm from 37 km^3 to 49 km^3 , or 2.6% of the Bering Strait freshwater delivery, which is very close to that for the heat flux. (We note that, unlike salinity, there was relatively little vertical structure in the temperature measured by the winched profiling device.)

Much has been made about the recent increase in the freshwater content of the Beaufort Gyre over the last decade. The Beaufort Gyre is the largest freshwater reservoir in the Arctic (Aagaard and Carmack, 1989), forced by the predominantly anti-cyclonic winds in the Canada Basin which tend to accumulate the freshwater from the periphery of the basin (Proshutinsky et al., 2002; Yang, 2006; Proshutinsky, 2009). A significant amount of the freshwater entering the gyre is driven by easterly winds in the Alaskan Beaufort Sea (Yang, 2006). In particular, upwelling favorable winds transport the fresh surface water offshore where it subsequently downwells due to Ekman pumping associated with the wind stress curl of the Beaufort High. Due to variations in the wind field over the western Arctic, the freshwater content of the gyre increases and decreases from year to year. In an anti-cyclonic wind regime the freshwater accumulates within the gyre, while under cyclonic wind forcing freshwater is released from the gyre (Proshutinsky et al., 2002). Because the atmospheric circulation has been more or less in an anti-cyclonic state since the late 1990s (Proshutinsky et al., 2011), the freshwater content of the gyre has increased significantly over this time period and now seems poised for a release. It has been hypothesized that such freshwater releases in the past have caused some of the great salinity anomalies that occur along the western margin of the North Atlantic (Dickson et al., 1988; Belkin et al., 1998).

The upwelling winds in the southern Canada basin are strongest during the fall and winter months, due to the increased sea level pressure gradient between the Beaufort High and the Aleutian Low (Yang, 2006). This is largely due to the seasonal deepening of the Aleutian Low (e.g. Favorite et al., 1976), which in turn is the integrated effect of individual low pressure systems progressing along the storm track of the north Pacific (e.g. Wilson and Overland, 1986; Zhang et al., 2004; Pickart et al., 2009a). As discussed earlier, the storm studied here is one of these Pacific cyclones whose

northern edge resulted in the enhanced easterly winds (Pickart et al., 2011). Hence it is of interest to assess the magnitude of the freshwater flux from the storm in terms of its contribution to the Beaufort Gyre freshwater inventory. Using annual hydrographic data collected in the Canada Basin, the freshwater storage of the gyre has been estimated over the period 2003–2010 (Proshutinsky, 2009; Proshutinsky, pers. comm., 2012). To compare with our off-shelf freshwater flux estimate, we consider the the upper 30 m of the gyre. The mean freshwater content over this depth is 3800 km^3 . This means that the storm in question fluxed the equivalent of 1.3% of the total inventory. However, the average yearly change in the freshwater content of the gyre over the 8-year period is 175 km^3 . This means that the individual storm could account for 28% of such year to year variation, which is indeed significant.

5.2. Nitrate and dissolved organic carbon fluxes

To estimate the fluxes of nitrate and dissolved organic carbon (DOC) during the storm, we used water sample data collected in the vicinity of the mooring array (see Section 2.2). The first step was to create a relationship between salinity and the variable in question. This was straightforward in both cases. For DOC there was a well-defined linear relationship such that the DOC decreases with increasing salinity. For nitrate the concentration increases from the fresh Alaskan Coastal Water into the saltier Pacific Winter Water, then decreases slightly into the underlying Atlantic Water (which is the saltiest). We computed a low-passed representation of this trend using the scatter of bottle data. Once these relationships were established, we converted the moored profiler salinity data (which included the synthesized data in the upper layer) into nitrate and DOC profiles, from which the mean fluxes of each quantity were calculated for the storm.

The mean profile of nitrate flux per unit depth and its vertical integral are shown in Fig. 16d. One sees the strong onshore flux of nitrate at depth associated mainly with the Pacific Winter Water (with some contribution from the Atlantic Water late in the storm). The net on-shelf flux of nitrate over the entire storm is $4.3 \times 10^9 \text{ mol}$. Such wind-driven transport of nitrate onto the shelf is likely an important mechanism for resupplying macro-nutrients that are exhausted during open water primary production. Primary production in the Beaufort Sea is nitrate-limited as the major source of nutrients to the western Arctic is through Bering Strait and most of these nutrients are utilized in the highly productive Chukchi Sea. If we assume 4–5 similar upwelling events each year, then the cumulative flux of nitrate onto the shelf is sufficient to support more than 80% of the $6\text{--}12 \text{ g C m}^{-2} \text{ year}^{-1}$ (e.g. Macdonald et al., 2010) of primary production that occurs on the Beaufort Shelf.

While the surface waters that are fluxed off the shelf during upwelling are nitrate-poor, they are fairly rich in DOC ($80\text{--}110 \text{ mol kg}^{-1}$) due to riverine discharge and some biological production (Mathis et al., 2005) over the shelf. During the storm in question there was a net off-shelf flux of DOC of $4.4 \times 10^9 \text{ mol}$. We note that this is roughly three times the amount of DOC carried offshore into the upper halocline by a cold core eddy that was observed in 2004 (Mathis et al., 2007). Because much of this DOC is of terrestrial origin and non-labile, it is entrained into the Beaufort Gyre and eventually exported from the Arctic Ocean (Benner et al., 2005). However, due to the extensive loss of sea ice in the Canada Basin in recent years, this organic matter is now being exposed to solar radiation during the summer and autumn months, which can allow for much faster breakdown. As the organic matter is remineralized by bacteria it increases carbon dioxide (CO_2) concentrations in the surface waters and could lead to outgassing events of CO_2 in regions that have traditionally been

a weak sink for atmospheric CO₂ (Bates and Mathis, 2009). This could have important consequences for regional carbon budgets.

5.3. Model parcel trajectories

We return now to the numerical model to investigate the three-dimensional pathways of the water during this type of upwelling event. As discussed above, in the observations the offshore Ekman transport at the shelf edge is balanced by onshore flow, but, unlike the two dimensional case for spatially uniform winds, the exchange in the model is a strong function of location along the boundary. The onshore transport on the western side (upstream, in a coastal wave sense) of the wind patch is smaller than the offshore Ekman transport, while the onshore transport on the eastern side (downstream) is larger than the Ekman transport. This is a consequence of the three-dimensional nature of the flow and the propagation of information from the westward limit of wind-forcing towards the east (e.g. Allen, 1976; Pickart et al., 2011). Note that this implies that the mooring array was located close to the region of peak winds (where the secondary flow was in fact approximately balanced).

A sense of the onshore and offshore flow, as well as the fate of the water being exchanged, can be demonstrated by calculating Lagrangian trajectories in the numerical model. A grid of simulated passive floats was initialized at 1300 km longitude (a bit east of the maximum wind, Fig. 3b). The pattern of float dispersal is similar at other longitudes, but the net displacements decrease for floats initialized farther to the west. The floats were advected by the three dimensional flow field for the 6 days of model integration using 3-D velocity data linearly interpolated between the Eulerian fields every 0.2 days. The initial starting positions of the floats are indicated on Fig. 17a by the asterisks, and the solid lines trace out the trajectories in the cross-stream plane (only

every other float is plotted here for clarity). One can see the offshore transport in the Ekman layer and the onshore transport at depth. Water is brought onto the shelf from below 150 m depth. Water at mid-depths off the shelf upwells about 25 m during the wind event, but returns to essentially the same depth as it started by the end of 6 days, resulting in an onshore shift of approximately 5 km. Much of the offshore region is characterized by a “sloshing” of water during the storm with very little net displacement. In contrast, parcels initially near the bottom over the shelf are carried far from their initial position.

The net displacement from the beginning to the end of the 6 day integration is shown in Fig. 17b–d for the floats initially at 1300 km longitude. Parcels near the surface are carried approximately 30 km in the offshore direction, and there is net offshore transport down to about 30 m depth (Fig. 17b). There is a region of large onshore transport centered near and just below the shelfbreak, where parcels initially at 40 km offshore are displaced more than 30 km onto the upper shelf. There is very little net meridional displacement for parcels below 200 m depth or offshore of 45 km (below the Ekman layer), although the depth-integrated onshore transport in the deep water exceeds the offshore Ekman transport. One sees that parcels initially in the lower part of the water column on the mid-shelf (between 10 and 20 km, Fig. 17b) show very little net meridional displacement, but do show a net vertical displacement of about 10–20 m (Fig. 17c). These floats were carried onshore, upwelled, and transported back offshore to near their original latitude. Vertical displacement is largest for those parcels initially just offshore of the shelfbreak, near 125 m depth (Fig. 17c). Water initially at this depth is upwelled over 100 m as it is advected onto the upper shelf.

Water parcels are also transported significant distances along the shelf. The zonal displacement (Fig. 17d) shows that floats initially at 1300 km longitude are advected as much as 300 km

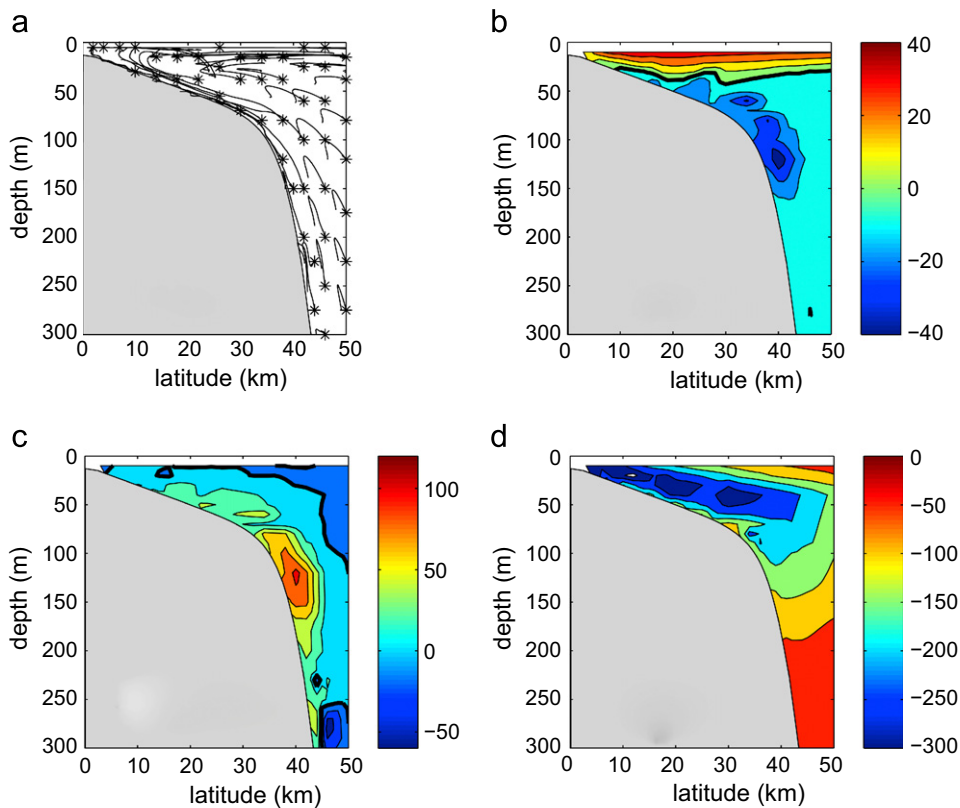


Fig. 17. (a) Lagrangian float trajectories from the numerical model in the y - z plane, initially located at $x=1300$ km. Asterisks mark the starting locations of the floats. Net displacement over the 6 days of model integration in the: (b) meridional (c.i.=10 m), (c) vertical (c.i.=20 m), and (d) zonal direction (c.i.=50 km).

towards the west, with the largest displacements found at mid-depths over the shelf. This is due to the westward flow resulting from the depression in sea surface height. Although the westward flow is strongest at the surface, those parcels are carried offshore by the Ekman transport, and so do not spend as much time in the westward current and experience less net zonal movement. These model zonal displacements serve as a reminder that the origin and fate of the water measured by the moorings is non-local, and that the heat and freshwater fluxed offshore in the vicinity of the array gets advected significantly to the west.

6. Conclusions

Our study of an autumn storm event has elucidated the dynamics of upwelling in the ice-covered waters of the Alaskan Beaufort Sea. The secondary (off-shelf) flow in the surface layer is consistent with Ekman theory when one takes into account the ice–ocean stress for the portion of the water column covered by freely moving pack-ice. This explains why Schulze and Pickart (2012) found that the upwelling response in general is strongest when there is partial ice cover (as opposed to near-100% ice cover when internal ice stress limits the transmission of wind energy into the ocean). The dynamics of the primary flow was addressed by evaluating the depth-integrated alongstream momentum equation. It was determined that, in the vicinity of the shelf edge, the divergence of cross-stream momentum flux helped drive the reversed upwelling jet. The subsequent spin-down of the jet (i.e. the re-establishment of the normal eastward-flowing shelfbreak current) was initiated by the alongstream pressure gradient. This occurred even before the easterly winds subsided.

Although there was no net transport of mass across the shelfbreak associated with the storm, there were substantial shelf–basin fluxes of heat, freshwater, and nitrate. The amount of heat transferred into the Canada Basin was comparable to the yearly supply of heat to the Beaufort shelf from the Pacific Water passing through Bering Strait. The quantity of freshwater fluxed off the shelf can account for a substantial fraction of the year-to-year variation in the freshwater inventory of the upper-layer Beaufort Gyre. And the flux of nitrate onto the shelf from the interior halocline waters could drive up to 25% of the primary productivity that occurs on the shelf. In recent years the atmospheric circulation in the Canada Basin has been predominantly anti-cyclonic (Proshutinsky et al., 2011), and there has been a summertime amplification of the Beaufort High (Moore, 2012). Together with more frequent and stronger high-latitude storms (e.g. Zhang et al., 2004) in a warming climate, this will likely result in more prevalent easterly winds in the region and therefore increased occurrences of upwelling. Consequently, the impacts described above are apt to become even more pronounced with greater influence on the ecosystem of the Alaskan Beaufort Sea and adjacent Canada Basin.

Acknowledgments

The authors thank Steve Lentz for helpful discussions during the course of the work. Andrey Proshutinsky provided information and insights about the Beaufort Gyre. Jack Cook and Terry McKee aided with some of the graphics. The following grants provided support for this study: National Science Foundation grant OPP-0731928 (R.P. and M.S.); National Science Foundation grant OPP-0713250 (R.P.); National Ocean Partnership Program project N00014-07-1-1040 (R.P.); and National Science Foundation grant ARC-1107997 (J.M.).

References

- Aagaard, K., 1984. The Beaufort Undercurrent, The Alaskan Beaufort Sea: Ecosystems and Environments. Academic Press, pp. 47–71.
- Aagaard, K., Carmack, E., 1989. The role of sea ice and freshwater in the Arctic circulation. *J. Geophys. Res.* 94, 14485–14498.
- Adcroft, A., Hill, C., Marshall, J., 1997. Representation of topography by shaved cells in a height coordinate ocean model. *Mon. Weather Rev.* 125, 2293–2315.
- Aksenov, Y., Ivanov, V., Nurser, A.J., Bacon, S., Polyakov, I.V., Coward, A.C., Naveira-Garabato, A.C., Beszczynska-Moeller, A., 2011. The Arctic circumpolar boundary current. *J. Geophys. Res.* 116, <http://dx.doi.org/10.1029/2010JC006637>.
- Allen, J.S., 1976. Some aspects of the forced wave response of stratified coastal regions. *J. Phys. Oceanogr.* 6, 113–119.
- Bates, N.R., Mathis, J.T., 2009. The Arctic Ocean marine carbon cycle: evaluation of air–sea CO₂ exchanges, ocean acidification impacts and potential feedbacks. *Biogeosciences* 6, 2433–2459.
- Belkin, I.M., Levitus, S., Antonov, J., Malmberg, S.-A., 1998. Great salinity anomalies in the North Atlantic. *Prog. Oceanogr.* 41, 1–68.
- Benner, R., Louchouart, P.L., Amon, R.W.W., 2005. Terrigenous dissolved organic matter in the Arctic Ocean and its transport to surface and deep waters of the North Atlantic. *Global Biogeochem. Cycles* 19, <http://dx.doi.org/10.1029/2004/GB002398>.
- Codispoti, L.A., Flagg, C., Kelly, V., Swift, J.H., 2005. Hydrographic conditions during the 2002 SBI process experiments. *Deep Sea Res.* 52, 3199–3226.
- Dickson, R.R., Meincke, J., Malmberg, S.-A., Lee, A.J., 1988. The “Great Salinity Anomaly” in the northern North Atlantic 1968–1982. *Prog. Oceanogr.* 20, 103–151.
- Favorite, F., Dodimead, A.J., Nasu, K., 1976. Oceanography of the subarctic Pacific region, 1962–72. *Bull. Int. North Pac. Comm.* 33, 1–187.
- Furey, P.W., 1996. The Large-scale Surface Wind Field Over the Western Arctic Ocean. Masters Thesis. University of Alaska, Fairbanks, AK, p. 121.
- Hibler, W.D., 1980. Modeling a variable thickness sea ice cover. *Mon. Weather Rev.* 108, 1943–1973.
- Hunkins, K.L., 1974. Subsurface eddies in the Arctic Ocean. *Deep Sea Res.* 21, 1017–1033.
- Karcher, M., Kauker, F., Gerdes, R., Hunke, E., Zhang, J., 2007. On the dynamics of Atlantic water circulation in the Arctic Ocean. *J. Geophys. Res.* 112, <http://dx.doi.org/10.1029/2006JC003630>.
- Large, W.G., McWilliams, J.C., Doney, S.C., 1994. Oceanic vertical mixing: a review and a model with a nonlocal boundary layer parameterization. *Rev. Geophys.* 32, 363–403.
- Lentz, S.J., Chapman, D.C., 2004. The importance of non-linear cross-shelf momentum flux during wind-driven coastal upwelling. *J. Phys. Oceanogr.* 34, 2444–2457.
- Lynch, A.H., Curry, J.A., Brunner, R.D., Maslanik, J.A., 2004. Toward and integrated assessment of impacts of extreme wind events on Barrow, Alaska. *Bull. Am. Meteorol. Soc.* 85, 209–221.
- Macdonald, R.W., Anderson, L.G., Christensen, J.P., Miller, L.A., Semiletov, I.P., Stein, R., 2010. Polar margins: the Arctic Ocean. In: Liu, K.K., et al. (Eds.), *Carbon and Nutrient Fluxes in Continental Margins: A Global Synthesis*. Springer, New York, pp. 291–303.
- Marshall, J., Hill, C., Perelman, L., Adcroft, A., 1997. Hydrostatic, quasi-hydrostatic, and non-hydrostatic ocean modeling. *J. Geophys. Res.* 102, 5733–5752.
- Mathis, J.T., Hansell, D.A., Bates, N.R., 2005. Strong hydrographic controls on spatial and seasonal variability of dissolved organic carbon in the Chukchi Sea. *Deep Sea Res.* 52, 3245–3258.
- Mathis, J.T., Pickart, R.S., Hansell, D.A., Kadko, D., Bates, N.R., 2007. Eddy transport of organic carbon and nutrients from the Chukchi shelf into the deep Arctic basin. *Journal of Geophysical Research*, 112, c05011, <http://dx.doi.org/10.1029/2006JC003899>.
- Mathis, J.T., et al., 2012. Storm-induced upwelling of high *p* CO₂ waters onto the continental shelf of the western Arctic Ocean and implications for carbonate mineral saturation states. *Geophys. Res. Lett.* 39, L07606, <http://dx.doi.org/10.1029/2012GL051574>.
- Moore, G.W.K., 2012. Decadal variability and a recent amplification of the summer Beaufort Sea High. *Geophys. Res. Lett.* 39, <http://dx.doi.org/10.1029/2012GL051570>.
- Nikolopoulos, A., Pickart, R.S., Fratantoni, P.S., Shimada, K., Torres, D.J., Jones, E.P., 2009. The western arctic boundary current at 152°W: structure, variability, and transport. *Deep Sea Res.* 56, 1164–1181.
- Pickart, R.S., 2004. Shelfbreak circulation in the Alaskan Beaufort Sea: mean structure and variability. *J. Geophys. Res.* 109, <http://dx.doi.org/10.1029/2003JC001912>.
- Pickart, R.S., Moore, G.W.K., Macdonald, A.M., Renfrew, I.A., Walsh, J.E., Kessler, W.S., 2009a. Seasonal evolution of Aleutian low-pressure systems: implications for the North Pacific sub-polar circulation. *J. Phys. Oceanogr.* 39, 1316–1339.
- Pickart, R.S., Moore, G.W.K., Torres, D.J., Fratantoni, P.S., Goldsmith, R.A., Yang, J., 2009b. Upwelling on the continental slope of the Alaskan Beaufort Sea: storms, ice, and oceanographic response. *J. Geophys. Res.* 114, C00A13, <http://dx.doi.org/10.1029/2008JC005009>.
- Pickart, R.S., Spall, M.A., Moore, G.W.K., Weingartner, T.J., Woodgate, R.A., Aagaard, K., Shimada, K., 2011. Upwelling in the Alaskan Beaufort Sea: atmospheric forcing and local versus non-local response. *Prog. Oceanogr.* 58, 78–100, <http://dx.doi.org/10.1016/j.pocean.2010.11.005>.

- Pickart, R.S., Pratt, L.J., Zimmermann, S., Torres, D.J., 2005. Flow of winter-transformed water into the western Arctic. *Deep Sea Res. II* 52, 3175–3198.
- Pickart, R.S., Spall, M.A., 2007. Impact of Labrador Sea convection on the North Atlantic meridional overturning circulation. *J. Phys. Oceanogr.* 37, 222–2207.
- Pickart, R.S., Spall, M.A., Torres, D.J., Moore, G.W.K., Moore, J.M.S., 2010. Upwelling in the Alaskan Beaufort Sea: forcing, dynamics, cross-stream fluxes, and biological implications. *EOS Trans. AGU* 91 (Ocean Sci. Meet. Suppl., Abstract IT14C-07).
- Pickart, R.S., Torres, D.J., Clarke, R.A., 2002. Hydrography of the Labrador Sea during active convection. *J. Phys. Oceanogr.* 32, 428–457.
- Pite, H.D., Topham, D.R., van Hardenberg, B.J., 1995. Laboratory measurements of the drag forces on a family of two-dimensional ice keel models in a two-layer flow. *J. Phys. Oceanogr.* 25, 3007–3031.
- Plueddemann, A., Krishfield, R., Edwards, C., 1999. Eddies in the beaufort gyre. In: *Ocean-Atmosphere-Ice Interactions (OAI) All Hands Meeting*.
- Proshutinsky, A., Bourke, R.H., McLaughlin, F.A., 2002. The role of the Beaufort Gyre in Arctic climate variability: seasonal to decadal climate scales. *Geophys. Res. Lett.* 29, <http://dx.doi.org/10.1029/2002GL015847>.
- Proshutinsky, A., et al., 2009. Beaufort Gyre freshwater reservoir: state and variability from observations. *J. Geophys. Res.* 114, C00A10, <http://dx.doi.org/10.1029/2008JC005104>.
- Proshutinsky, A., et al., 2011. The Arctic Ocean (in state of the climate in 2010). *Bull. Am. Meteorol. Soc.* 92, 145–148.
- Roach, A.T., Aagaard, K., Pease, C.H., Salo, S.A., Weingartner, T.J., Pavlov, V., Kulakov, M., 1995. Direct measurements of transport and water properties through the Bering Strait. *J. Geophys. Res.* 100, 18443–18457.
- Rudels, B., Jones, E.P., Anderson, L.G., Kattner, G., 1994. On the intermediate depth waters of the arctic ocean. The polar oceans and their role in shaping the global environment. *Geophys. Monogr.* 85, 33–46.
- Schulze, L.M., Pickart, R.S., 2012. Seasonal variation of upwelling in the Alaskan Beaufort Sea: Impact of sea ice cover. *J. Geophys. Res.* 117, C06022, <http://dx.doi.org/10.1029/2012JC007985>.
- Spall, M.A., Pickart, R.S., Fratantoni, P.S., Plueddemann, A.J., 2008. Western arctic shelfbreak eddies: formation and transport. *J. Phys. Oceanogr.* 38, 1644–1668.
- Steele, M., Zhang, J., Ermold, W., 2010. Mechanisms of summertime upper arctic ocean warming and the effect on sea ice melt. *J. Geophys. Res.* 115, <http://dx.doi.org/10.1029/2009JC005849>.
- Sutherland, D.A., Pickart, R.S., 2008. The East Greenland coastal current: structure, variability and forcing. *Prog. Oceanogr.* 78, 58–77, <http://dx.doi.org/10.1016/j.pocean.2007.09.006>.
- Suydam, R.S., 2009. Age, Growth, Reproduction, and Movements of Beluga Whales (*Delphinapterus leucas*) from the Eastern Chukchi Sea. Ph.D. Thesis. University of Washington, Seattle, WA, 152 pp.
- Timmermans, M.L., Toole, J., Proshutinsky, A., Krishfield, R., Plueddemann, A., 2008. Eddies in the Canada Basin, Arctic Ocean, observed from ice-tethered profilers. *J. Phys. Oceanogr.* 38, 133–145.
- Tsubouchi, T., et al., 2012. The Arctic Ocean in summer: a quasi-synoptic inverse estimate of boundary fluxes and water mass transformation. *J. Geophys. Res.* 117, <http://dx.doi.org/10.1029/2011JC007174>.
- von Appen, W.-J., Pickart, R.S., 2012. Two configurations of the western Arctic shelfbreak current in summer. *J. Phys. Oceanogr.* 42, 329–351.
- Weingartner, T.J., Cavalieri, D.J., Aagaard, K., Sasaki, Y., 1998. Circulation, dense water formation, and outflow on the northeast Chukchi shelf. *J. Geophys. Res.* 103, 7647–7661.
- Williams, W.J., Carmack, E.C., Shimada, K., Melling, H., Aagaard, K., Macdonald, R.W., Ingram, R.G., 2006. Joint effects of wind and ice motion in forcing upwelling in Mackenzie Trough, Beaufort Sea. *Cont. Shelf Res.* 26, 2351–2366.
- Wilson, J.G., Overland, J.E., 1986. Meteorology. The Gulf of Alaska. In: Hood, D.W., Zimmermann, S.T. (Eds.), *Physical Environment and Biological Resources*. Alaska Office, Ocean Assessments Division, National Oceanic and Atmospheric Administration, US Department of Commerce, pp. 31–54.
- Woodgate, R.A., Aagaard, K., Muench, R.D., Gunn, J., Björk, G., Rudels, B., Roach, A.T., Schauer, U., 2001. The Arctic Ocean boundary current along the Eurasian slope and the adjacent Lomonosov Ridge: water mass properties, transports, and transformations from moored instruments. *Deep Sea Res.* 48, 1757–1792.
- Woodgate, R.A., Aagaard, K., Weingartner, T.J., 2006. Interannual changes in the Bering Strait fluxes of volume, heat and freshwater between 1991 and 2004. *Geophys. Res. Lett.* 33, L15609, <http://dx.doi.org/10.1029/2006GL026931>.
- Yang, J., 2006. The seasonal variability of the Arctic ocean Ekman transport and its role in the mixed layer heat and salt fluxes. *J. Clim.* 19, 5366–5387.
- Zhang, X., Walsh, J.E., Zhang, J., Bhatt, U.S., Ikeda, M., 2004. Climatology and interannual variability of arctic cyclone activity: 1948–2002. *J. Clim.* 17, 2300–2317.